Uniaxial constitutive model for fiber reinforced concrete: A physics-based data-driven framework

Chunlei Yu [a], Min Yu [a *], Xiangyu Li [a], Lihua Xu [a], Sumei Liu [a], Jianqiao Ye [b]
[a] School of Civil Engineering, Wuhan University, Wuhan, Hubei Province 430072, China
[b] School of Engineering, Lancaster University, Lancaster LA1 4YR. UK

Abstract: Fiber reinforced concrete (FRC) has improved strength and ductility, making it suitable for a wider range of engineering structures. The development of a constitutive model is crucial for analyzing mechanical behavior of these structures, while this still remains challenging as the complex composition of FRC makes it difficult to formulate explicit relationships among a range of critical material parameters. With the latest development of data and digital technologies, data-driven approaches have emerged as a powerful alternative that are capable of solving advanced and complex engineering problems. Developing data-driven methods based on objective data analysis and decision-making to predict mechanical behavior of engineering structures is an important direction of such development. In this paper, a uniaxial constitutive model of fiber-reinforced concrete is developed by a physics-based data-driven framework. The framework consists of three important parts, including construction of experimental database, parameters calibration of physical models, and implementation of neural network. From the experimental data collected from published literature, an experimental database is built first. A physical model is proposed by modifying the uniaxial constitute model for normal concrete, so that it is more convenient and straightforward to consider the effect of fibers on fiber reinforced concrete subjected to compression, tension and repeat loading conditions. The parameters of the model are calibrated against experimental data by the swarm intelligence optimization algorithms. With the calibrated parameters of the physical model, a Fully Connected Neural Network (FCNN) is trained to be used to predict the physical parameters of fiber reinforced concrete. By comparing with independent experimental data, the proposed fiber-reinforced concrete uniaxial constitutive model constructed using the physics-based data-driven framework can accurately predict the stress-strain relationships of a range of FRC, which suggests that the FRC material model can be used in the numerical simulation and design of FRC components and structures. In addition, the proposed model is applicable to multiple loading conditions.

Keywords: Uniaxial constitute model, Fiber reinforced concrete, Data-driven, Neural network, Database

1. Introduction

To address the issues of low tensile strength [1], brittleness, and poor durability of normal concrete (NC), various reinforcement techniques have been employed over the past few decades. Among these techniques, fiber reinforcement has emerged as one of the most effective approaches for enhancing the properties of concrete. When external forces act upon a fiber reinforced composite (FRC), the fibers form a bridge-like structure that encloses cracks, effectively slowing or preventing further crack propagation. This bridging effect absorbs energy, distributes load, and significantly reduces crack width. All of these have been observed by Xu[4] who conducted microphotography of FRC specimens after mechanical testing, which shown debonding of steel fiber and relative sliding with detached matrix adhered to the fiber surface. The macro-level compressive and tensile properties of FRC are greatly improved due to the micro-level fiber-bridge behavior. Specifically, the compressive and tensile strength and elastic modulus of FRC are increased. Moreover, the failure mode of FRC changes from sudden brittle failure to continuous cracking, resulting in a transition from brittleness to pseudo-ductility[5]. Consequently, the residual strength of FRC, particularly in tension, is significantly increased. This allows FRC to withstand large deformations and makes it an ideal material for structures in disastrous situations, such as

earthquakes. Structures constructed with FRC also exhibit excellent mechanical performance, including high strength capacity[6,7], ductile failure modes[8], and considerable residual capacity[9]. As a result, FRC has been increasingly used as a construction and building material.

Constitutive model is a fundamental property of a material and serves as the basis for numerical simulations. OpenSees[10] offers various empirical uniaxial constitutive models for normal concrete (NC), such as Concrete01-Concrete07. Compared to the uniaxial constitutive model of NC, the uniaxial stress-strain curve of FRC has three distinct properties, *i.e.*, higher peak stress, continuous and smooth stress reduction after reaching the peak, and a significant residual stress with a large strain, particularly in tension. To consider these properties, Gao[11] proposed an compressive empirical uniaxial constitutive model for FRC based on Guo's model[12] for NC. The parameters of the proposed model were calibrated by compressive experiments of FRC, of which a parameter, named fiber feature index, was used to consider the fiber effect. For concrete reinforced with steel and polypropylene fibers and subjected to repeat load patterns, Li[13] observed a significant effect of fibers on the residual plastic strain and developed two empirical split uniaxial models for FRC under repeat compression and tension. The proposed uniaxial constitutive models can effectively describe the mechanical behavior of fiber-reinforced concrete (FRC) subjected to compression or tension. To the authors' best knowledge, the constitutive models of FRC available in the literature were developed independently for specific constituents and loading conditions. Thus, a change of fiber contents or loading conditions will normally require new experimental tests to calibrate some of the critical material parameters that are essential to define the loading and unloading paths of the constitutive law, which is obviously expensive and time consuming. There is, therefore, an urgent demand for an approach that may simplify the process and provide a useful and practical tool to construct constitutive models for a range of FRC.

Currently, the exponential growth of data and rapid advancements in computer and computational technologies have led to a shift from the traditional model-centric approach to a data-centric approach. Consequently, the extraction of valuable information from vast amounts of data has become increasingly crucial. Various models[14], such as Support Vector Machines (SVM), Decision Trees (DT), Artificial Neural Networks (ANN), and Evolutionary Algorithms, have been employed to predict concrete properties. Compressive strength[15–32], which is one of the most important properties of concrete, has received the greatest attention as the primary target for data-driven approaches. For example, machine learning (ML) methods have been used to predict elastic modulus[33–36] of given concrete compositions. Using concrete compositions as inputs, ML methods were also used to predict splitting tensile strength[37], flexural strength[38], and shear strength[39]. In addition to predicting material properties, there have been attempts to determine strain-stress relationship of concrete using ML methods. Zhou[40] utilized GoogLeNet, AlexNet, VGGNet, and ResNet, which are pixel-to-pixel ML models, to predict strain-stress relationships from meso-model images. Apart from the pixel-based learning, Zhang[41] employed Long Short-Term Memory (LSTM), a sequence-to-sequence model, to simulate the stress-strain behavior of soil. In comparison to the pixel-to-pixel models, the sequence-to-sequence model offers a more straightforward approach. Currently, these ML models trained directly from data can provide accurate predictions for FRC under simple loading conditions, such as monotonic loads, thought when the loadings become more complex, such as repeated loading, a model trained entirely from data may not be sufficiently accurate. Nevertheless, the above literature has shown that a data-driven approach, such as a ML model, has great potential to be trained to predict critical material parameters of FRC with a range of different fiber reinforcement and concrete compositions, and potentially for various loading conditions.

In this paper, we develop a uniaxial constitutive model for FRC using a hybrid framework that combines physics-based principles with data-driven techniques. This model is designed to accurately capture the behavior of fiber reinforced concrete subjected to a wide range of loading patterns. The model takes concrete mixture and strain path of concrete, which are presented by a number of critical strain parameters, as inputs and the outputs are the predicted critical stresses along the stress path. To complete the hybrid data training process, a modified version of the uniaxial constitutive model ConcreteCM, where CM represents Chan and Mander who proposed the model[42], is developed as the physics model.

ConcreteCM has a distinctive post-peak quasi-plastic loading path in comparison to some other models with abrupt stress drop and is capable of describing the stress-strain relation of FRC. However, when a FRC is subjected to a repeated load, the fiber properties and contents have significant impacts on the residual strain that plays an important role in the cyclic analysis. Unfortunately, the residual plastic strain of original ConcreteCM is properties-dependent, which limit the capacity to specify the relationship between residual plastic strain and concrete mixtures. To address this limitation, a modification is made to ConcreteCM in this paper to calculate the mixture-dependent residual plastic strain. The modified model, referred to as ConcreteCMM, is defined by 10 parameters, including peak strain $\varepsilon_c(\varepsilon_t)$, peak stress $\sigma_c(\sigma_t)$, elastic module $E_c(E_t)$, shape factor $r_c(r_t)$, unload and reload factor $ulp(ult)$ for the compressive (tensile) branch. As expected, explicit relationships between concrete mixture and these parameters are difficult to found and most likely do not exist. Alternatively, as discussed previously in the literature review, a data-driven approach may be implemented to tackle this challenging and practically important problem.

In the proposed data-driven framework, a Fully Connected Neural Network (FCNN) is trained to perform this task. Prior to the training, an optimization algorithm with a strategy is adopted to obtain the parameters of ConcreteCMM from the corresponding stress-strain experimental curves. This provides a data source for training the FCNN. Once the FCNN is trained, it takes concrete mixture as inputs and outputs the corresponding parameters of ConcreteCMM. The obtained critical parameters of the strain path is input into ConcreteCMM to predict the parameters of the stress path. Thus, in comparison with the existing FRC models, the new model, ConcreteCMM built from the FCNN trained parameters, can be used to predict the stress-strain behavior of FRC with consideration of the influence of fibre contents and concrete mixtures for a range of loading conditions, including compression, tension and repeated loading.

2. Development of database for fiber-reinforced concrete

2.1. Database design

Experiment is regarded as the most traditional and reliable way of scientific research. For a data-driven framework, creation of experimental database is essential, which includes efficiency of data retrieving and saving. Performance of a database depends on its design, in which data relevance and redundancies are two key factors[43,44]. In a typical mechanical experiment on fiber reinforced concrete, there are two separated stages, i.e., specimen production and loading. At the specimen production stage, the recorded data include material sources, specimen geometry, and concrete mixture, etc. At the loading phase, data such as loading patterns and all the mechanical measurements are recorded.

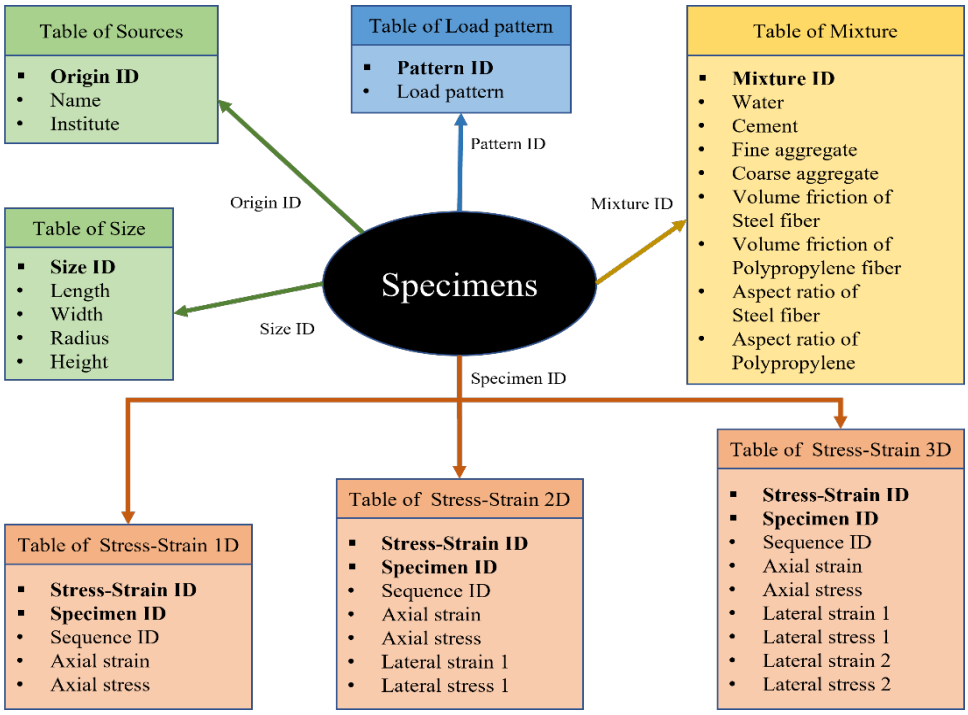

Figure 1. Design of Experimental Database for FRC

As shown in Figure 1, eight tables are designed in the database. The specimen table is the main index table, which is connected to all other tables by multiple keys. Mixture of the specimen can be retrieved from the Mixture table by the mixture ID. Similarly, size, sources, and load patterns of the specimen can be fetched from their respective Tables by Size ID, Origin ID, and Pattern ID. For the experimental data, the stress strain curve of a specimen can be obtained from the Stress-Strain Table through Specimen ID. It is worthy of noting that the Sequence ID is introduced to ensure that the location where a strain-stress curve is measured is arranged in a desired sequence.

2.2. Database visualization

After completing the design, the collected data need to be checked and imported into the database. The data can be analyzed by a visualization system that is developed specifically for this purpose. This visualization system is developed using the PySide6 open sources third-party library. To ensure an effective and reliable storage structure of the experimental data, PostgreSQL is chosen as the database system. The Graphical user interface (GUI) of the visualization system is shown in Figure 2.

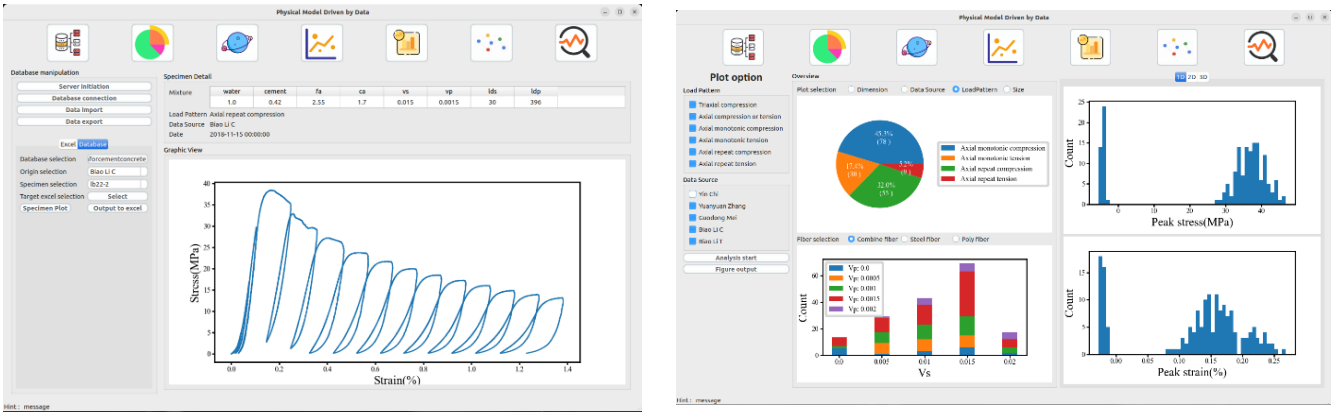

a) Visualization of specimen b) Analysis and visualization of the database

Figure 2. The Graphical user interface (GUI) of the visualization system

In Figure 2(a), there are four long buttons on the upper left panel designed for, respectively, server initiation, database

connection, data import, and data export. Below the database manipulation panel are two sub-tabs, i.e., the Excel and Database tabs, for selecting source of data to be plotted, imported, or removed. Two sections are designed in the main view section of the GUI, i.e., the Specimen Detail and the Graphic View sections. Once a specimen is selected from the left panel, the mixture, load pattern, source, and experimental data of the chosen specimen will be shown in the Specimen Details section and the stress-strain curve will be plotted in the Graphic view section.

After importing the collected data into the database, data visualization is necessary to identify patterns, trends, and outliers, as shown in Figure 2(b). On the left of the visualization screen, the plot options menu offers selections of load patterns and data sources. The main view panel shows the distribution of the selected features of the specimen, including load patterns, fiber volume ratios, peak stresses, and peak strains.

With the help of the graphical representation of data, such as the charts and the graphs shown in Figure 2, the trends, outliers and patterns of the collected data can be easily understood. The developed visualizations system can also facilitate data importing and exporting.

2.3. Analysis of the collected data in the database

The data sources are shown in Table 1. Using the visualization system developed in Section 2.2, graphic views of the relevant data for all the specimens in the database are shown in Figure 2. The data of a variety of fibers were collected from literature, including hooked-end, straight, and corrugated steel fibers with fiber ratios of 40, 60, and 80, as well as monofilament polypropylene fibers with a fiber ratio of 280. In terms of load patterns, of the specimens in the database, 62.7% are compressive specimens, and 37.3% are tensile specimens. Among the compressive specimens, 72.2% of them are subjected to monotonic compression, while the remaining 27.8% are subjected to non-monotonic compression. For the distribution of fibers, shown in Figure 3, the volume fraction of steel fibers ranges from 0 to 2% and the volume fraction of polypropylene fibers ranges from 0 to 0.2%. Within the database, most of the specimens have a steel fiber fraction of 1.5%, while for PP fiber fraction, the percentage is 0.15%. The average aspect ratios of the steel fibers in the database are grouped by 30, 60 and 80, respectively. The aspect ratios of polypropylene fibers are 167, 280 and 396, in which the fibers of most of the specimens have an average ratio of 396. The distribution of peak stress and peak strain clearly shows that the specimens are under either tension or compression.

Table 1. Data source

Reference	Load pattern	No. of specimen
Yuanyuan Zhang[45]	Axial monotonic compression	78
Guodong Mei[46]	Axial monotonic tension	30
Biao Li[13]	Axial non-monotonic compression	55
Biao Li[13]	Axial non-monotonic tension	9

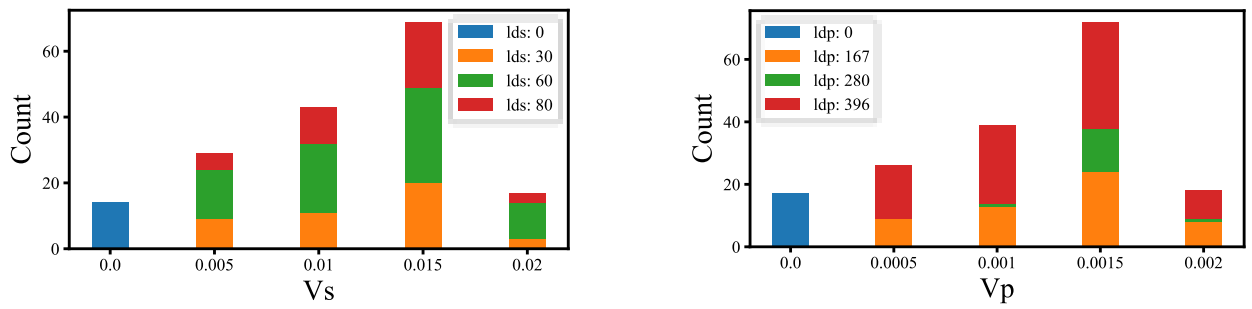

a) Distribution of steel fibers b) Distribution of polypropylene fibers

Figure 3. Fiber distribution of the specimens

Among all the 133 compressive specimens in the database, as presented in Figure 4, the visualization shows that there are 78 specimens subjected to monotonic compression, accounting for 58.6% of the total compressive specimens, and 55 specimens are subjected to non-monotonic compression, accounting for 41.4% of the total compressive specimens. The peak stresses of all the specimens are between 28MPa and 47Mpa. The distribution of peak strains is similar to that of the peak stresses, and ranges from 0.08% to 0.27%.

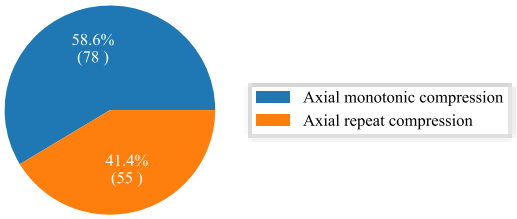

a) Distribution of load pattern

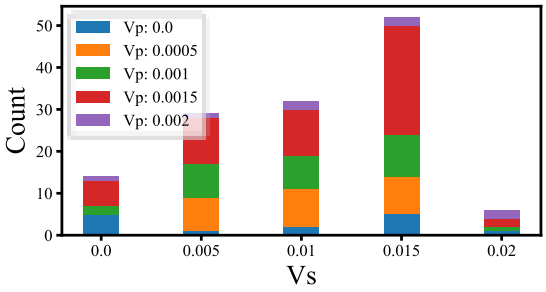

b) Distribution of steel and polypropylene fiber in volume fraction

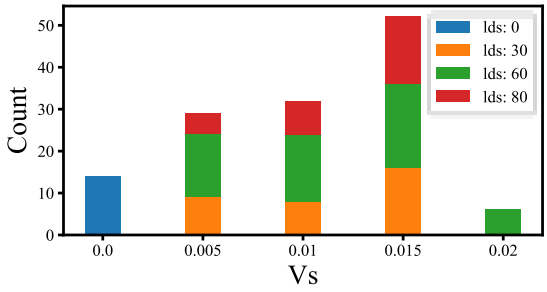

c) Distribution of steel fiber in volume fraction and aspect ratio

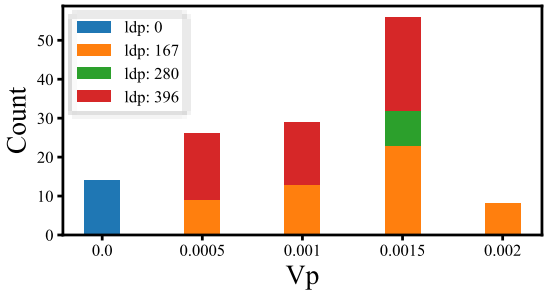

d) Distribution of polypropylene fiber in volume fraction and aspect ratio

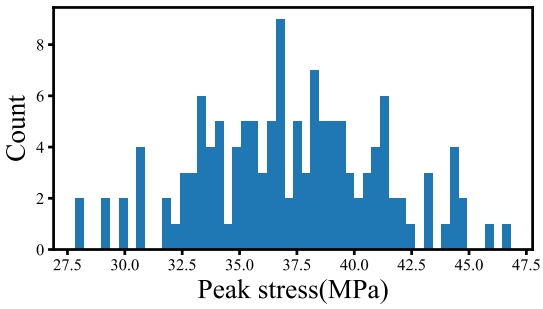

e) Distribution of peak strain

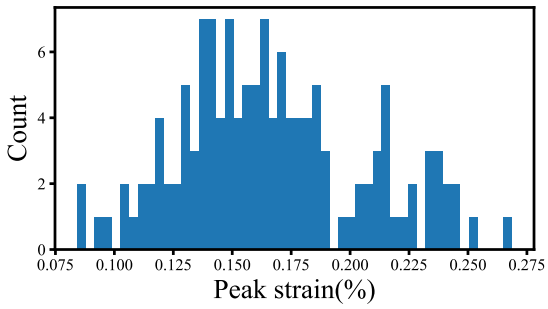

f) Distribution of peak stress

Figure 4. Overview of the collected uniaxial compressive specimens

The graphic analyses of all the 39 specimens in tension are shown in Figure 5. There are 30 specimens subjected to monotonic tension and 9 subjected to non-monotonic tension, accounting for 76.9% and 23.1% of the total tensile specimens, respectively. All tensile specimens have steel fibers only. The volume fraction of steel fibers ranges from 1% to 2%. The peak stresses are relatively low, within the range of 3Mpa to 6Mpa. The peak strains are mostly around 0.0225%. With added fibers, the tensile peak stress is greater than one-tenth of the compressive peak stress, which ranges from 28Mpa to 47Mpa, indicating effective tensile reinforcement.

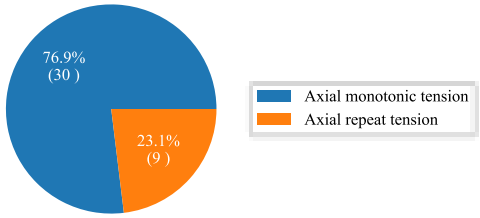

a) Distribution of load pattern

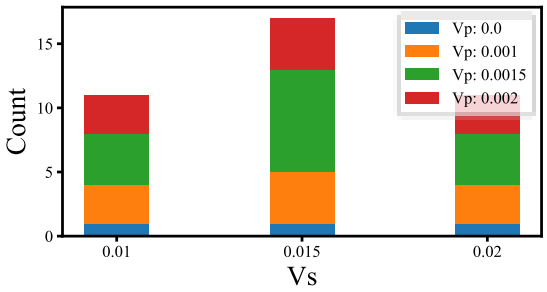

b) Distribution of steel and polypropylene fiber in volume fraction

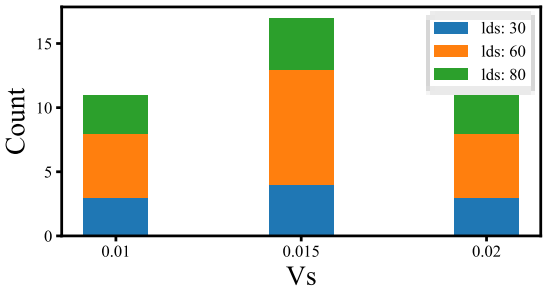

c) Distribution of steel fiber

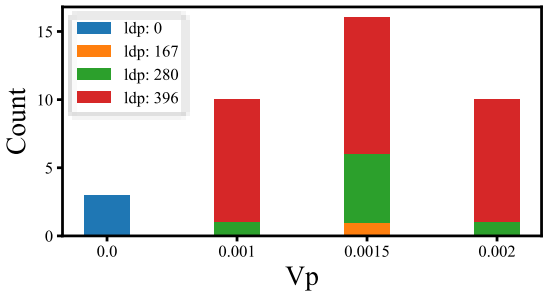

d) Distribution of polypropylene fiber

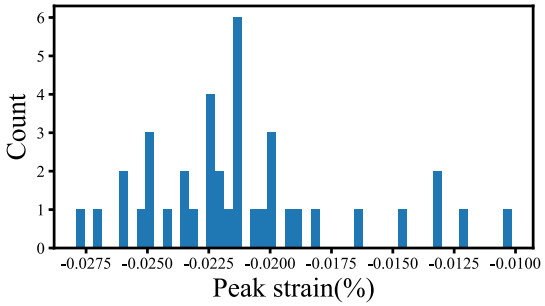

e) Distribution of peak strain

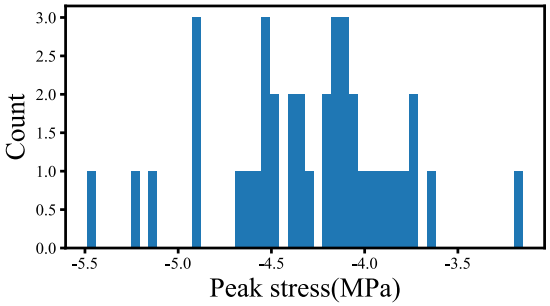

f) Distribution of peak stress

Figure 5. Overview of collected uniaxial tensile specimens

In the previous research and the code of normal concrete, compressive strength is typically chosen as the primary parameter. Other mechanical properties, such as elastic modulus and peak strain, are then calculated based on the compressive strength. In this data-driven study, which is for fiber-reinforced concrete (FRC), a statistical analysis is conducted to evaluate possible correlations among the mechanical properties. For both compression and tension, the elastic modulus is calculated as the slope of the secant line between the 0.4 peak stress and the 0.2 peak stress on the stress-strain curve. The peak stress and peak strain are determined as the highest stress and the correspond strain on the stress-strain curve. Two evaluation criteria, i.e., the maximal information coefficient (MIC) and the correlation coefficient rare used here to estimate the degree of correlation quantitatively. The correlation coefficient r can capture the degree of the linear relationship between variables, while the MIC can be used to include some nonlinear effects[47]. As shown in Figure 6a), the MIC and r between elastic module and compressive peak stress are 0.25 and 0.21, respectively, for specimens subjected to non-monotonic compression. The MIC and r rise to 0.51 and 0.66, respectively, for repeated loading, suggesting an increased linear correlation. The compressive peak strain is negatively proportional to the compressive peak stress with an r at -0.53 for the specimens subjected to non-monotonic compression. The tensile peak stress does not exhibit a clear

correlation with the compressive peak stress.

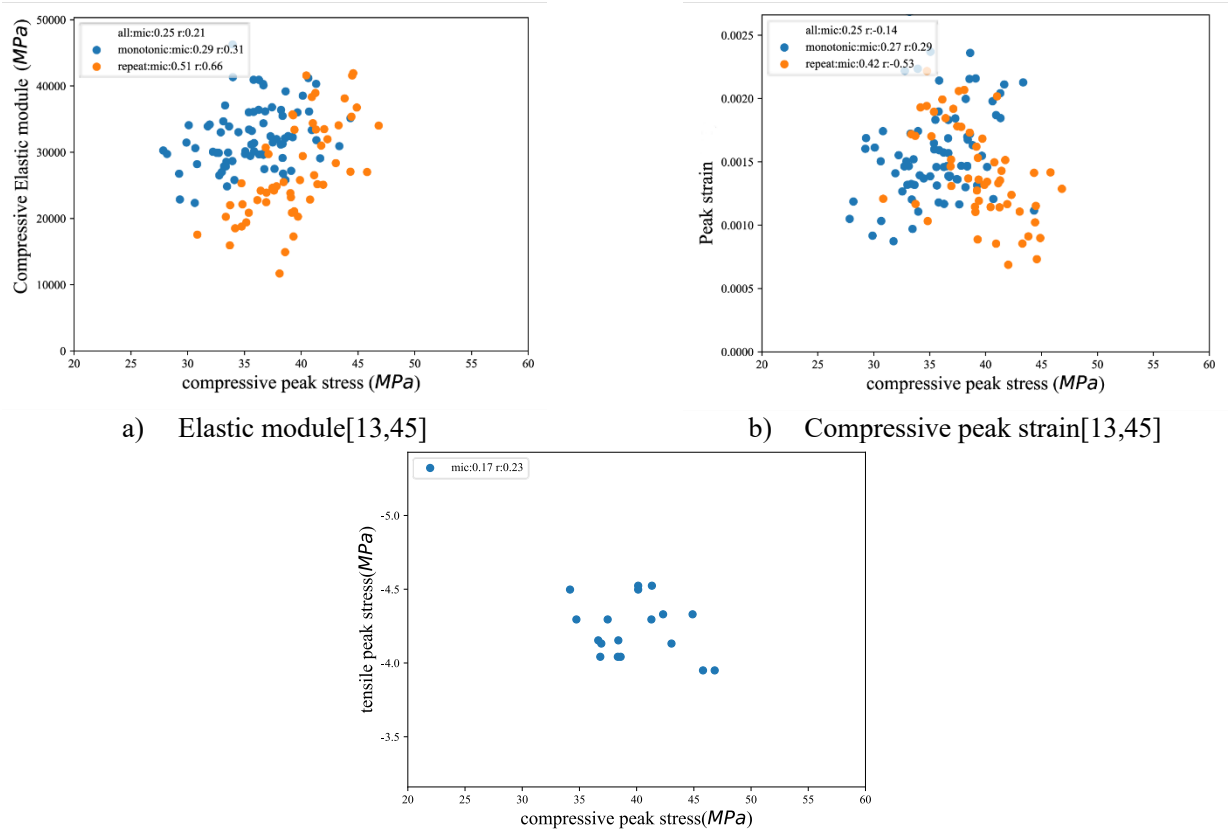

a) Elastic module[13,45] b) Compressive peak strain[13,45]

c) Tensile peak stress[45,45,46]

Figure 6. Correlation analysis of mechanical parameters vs compressive peak stress

The low r and MIC values in Figure 6 indicate that explicit mathematical equations defining the relationships among the important mechanical properties are difficult to be formulated. Thus, a data-driven approach is a useful alternative that may be more appropriate for specifying the intrinsic relationships among the mechanical parameters.

3. Physics-based data-driven model

3.1. A framework of physics-based data-driven model

A physics-based data-driven framework is proposed here to build a uniaxial constitute model for fiber-reinforced concrete. The key steps of the framework are discussed in detail below. Figure 7 shows the physics-based data-driven framework, which includes three parts, i.e., physics model parameter calibration and optimization algorithm, establishment of fully connected neural networks, and formation of experimental database of fiber-reinforced concrete.

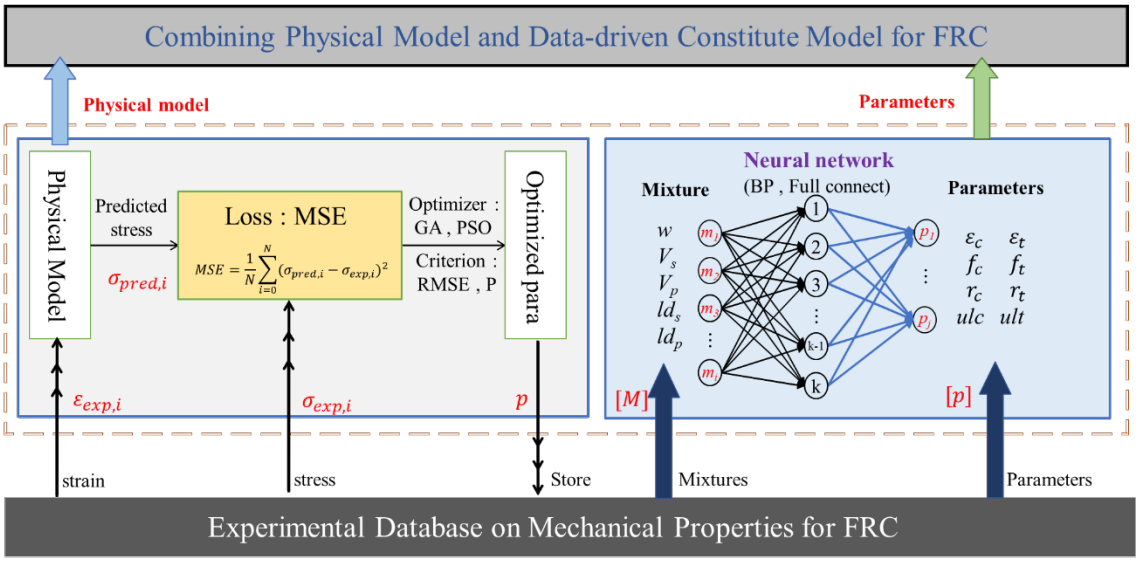

Figure 7. The framework of physics-based data-driven model

The experimental database provides data for parameter calibration and neural network training. For the physical model parameters calibration, swam intelligent optimization algorithms are applied to find optimal parameters of the physical model that fits the experimental data. Finally, fully a connected neural network is trained to find the relationship between the concrete mixture and the calibrated parameters of the physical model.

By parameter calibration, stresses can be predicted from the experimental strains by using the physical model. Mean squared error (MSE) is applied as the loss function to evaluate the error between the predicted stresses and the stresses from experiments. Genetic algorithm (GA) and particle swimming optimization algorithm (PSO) are used to find the minimum of the loss function, resulting in optimized physics model parameters that provide the best possible fit to the experimental stress-strain curve. Finally, the parameters of the optimized physics model are used to update the database.

To establish the network, a fully connected neural network is selected. The concrete mixture and the optimized physical model parameters are taken as the input and output of the neural network, respectively. After training the network with the data, the neural network can effectively predict all the physics model parameters for a given concrete mixture. More details of the neural network are presented in 3.3.1.

Once the model parameters are predicted by the trained network, the physics model of the concrete is uniquely defined and the final strain-stress curve of the concrete can be plotted.

3.2. Parameter calibration of physical model

On the system interface shown in Figure 7, there are three key parts, i.e., physics model, loss function, and optimization. MSE is chosen as the loss function to measure the error between the predicted and the experimental strain stress curves. For the physics model and the optimization, the details are shown below.

3.2.1. Physical model for fiber-reinforced concrete

There have been some uniaxial constitutive models for fiber-reinforced concrete. Gao [11] used the fiber feature index to consider the effect of steel fibers and proposed a uniaxial monotonic compressive model. Based on Gao's model, Shi[48] introduced a trilinear uniaxial monotonic tensile stress-strain relationship for fiber-reinforced concrete; Li[13] applied different models for uniaxial cyclic tension and compression of fiber-reinforced concrete. It is clear from the above constitutive models, there is not a unified model that are applicable to a range of load patterns.

It has been verified that the skeleton curve of a FRC under cyclic load is very close to the stress-strain curve of the FRC under monotonic load[49–52]. There are a number of equations[53–58] that can be used to plot stress-strain curve of

concrete under a monotonic load, among which Tsai's[58] equation has well-defined ascending and descending branches which makes is suitable to describe the uniaxial mechanical behavior of concrete. Tsai's equation is shown in Eq. (1),

$$y = \frac{nx}{1 + \left(n - \frac{r}{r-1}\right)x + \frac{x^r}{r-1}} \qquad \begin{matrix} \text{where, } x = \frac{\varepsilon}{\varepsilon_c}, y = \frac{\sigma}{f_c}, n = \frac{E_c \varepsilon_c}{f_c} \text{ for compression} \\ x = \frac{\varepsilon}{\varepsilon_t}, y = \frac{\sigma}{f_t}, n = \frac{E_t \varepsilon_t}{f_t} \text{ for tension} \end{matrix} \tag{1}$$

In Eq.(1), $\varepsilon_c(\varepsilon_t), f_c(f_t)$ and $E_c(E_t)$ are peak strain, peak stress and initial elastic module of concrete under compressive (tensile) load, respectively. $r_c(r_t)$ and $n_c(n_t)$ are two factors that determine the shape of the compressive (tensile) curve. The skeleton curve of ConcreteCM is shown in Figure 8(a), where ε and σ are strain and stress.

Based on the skeleton curve (Eq.1) proposed by Tsai, Chang and Mander [22] introduced unloading and reloading in their constitutive model, namely ConcreteCM, so that the model can be used to simulate the responses of materials subjected to repeated compressive and tensile loads. Equations (2) and (3) show the calculation of the unloading and reloading curves, as illustrated in Fig.8(a) and Fig. 8(b). |In the following sections. The loading point $(\sigma_{un}, \varepsilon_{un})$ is replaced by $(\sigma_{unc}, \varepsilon_{unc})$ and $(\sigma_{unt}, \varepsilon_{unt})$, respectively, for compression and tension. Similarly, the respective residual plastic strains, ε_{pl}, are denoted as ε_{plc} and ε_{plt}. To specify the unloading and reloading process, four elastic moduli are required, *i.e.*, the initial unloading modulus E_0, the unloading plastic modulus E_{pl}, the unloading secant modulus E_{sec}, and the reloading modulus E_{new}. A reloading process is considered complete when the strain reaches the unloading strain (ε_{un}), at which the correspond stress decreases by $\Delta\sigma$.

	Compression	Tension	
Unloading curve	$\sigma = E_0(\varepsilon - \varepsilon_{plc}) + A(\varepsilon - \varepsilon_{plc})^B$	$\sigma = E_0(\varepsilon - \varepsilon_{plt}) + A(\varepsilon - \varepsilon_{plt})^B$	(2)
	$A = \frac{E_{sec} - E_{pl}}{(\varepsilon_{unc} - \varepsilon_{plc})^{B-1}}$	$A = \frac{E_{sec} - E_{pl}}{(\varepsilon_{unt} - \varepsilon_{plt})^{B-1}}$	
	$B = \frac{E_0 - E_{pl}}{E_{sec} - E_{pl}}$	$B = \frac{E_0 - E_{pl}}{E_{sec} - E_{pl}}$	
	$E_0 = E_c$	$E_0 = E_t$	
	$E_{pl} = \frac{E_c}{\lvert\frac{\varepsilon_{unc} - \varepsilon_0}{\varepsilon_c}\rvert^{1.1} + 1}$	$E_{pl} = \frac{E_t}{\lvert\frac{\varepsilon_{unt} - \varepsilon_0}{\varepsilon_t}\rvert^{1.1} + 1}$	
	$\varepsilon_{plc} = \varepsilon_{unc} - \frac{\sigma_{unc}}{E_{sec}}$	$\varepsilon_{plt} = \varepsilon_{unt} - \frac{\sigma_{unt}}{E_{sec}}$	
	$E_{sec} = E_c\left(\frac{\lvert\frac{\sigma_{unc}}{E_c\varepsilon_c}\rvert + 0.57}{\lvert\frac{\varepsilon_{unc}}{\varepsilon_c}\rvert + 0.57}\right)$	$E_{sec} = E_c\left(\frac{\lvert\frac{\sigma_{unt}}{E_c\varepsilon_t}\rvert + 0.67}{\lvert\frac{\varepsilon_{unt} - \varepsilon_0}{\varepsilon_t}\rvert + 0.67}\right)$	
Reloading curve	$\sigma = E_{new}(\varepsilon - \varepsilon_{plc})$	$\sigma = E_{new}(\varepsilon - \varepsilon_{plt})$	(3)
	$E_{new} = \frac{\sigma_{new}}{\varepsilon_{unc} - \varepsilon_{plc}}$	$E_{new} = \frac{\sigma_{new}}{\varepsilon_{unt} - \varepsilon_{plt}}$	
	$\Delta\sigma = 0.09\sigma_{unc}\sqrt{\lvert\frac{\varepsilon_{unc}}{\varepsilon_c}\rvert}$	$\Delta\sigma = 0.15\sigma_{unt}$	
	$\sigma_{new} = \sigma_{unc} - \Delta\sigma$	$\sigma_{new} = \sigma_{unt} - \Delta\sigma$	

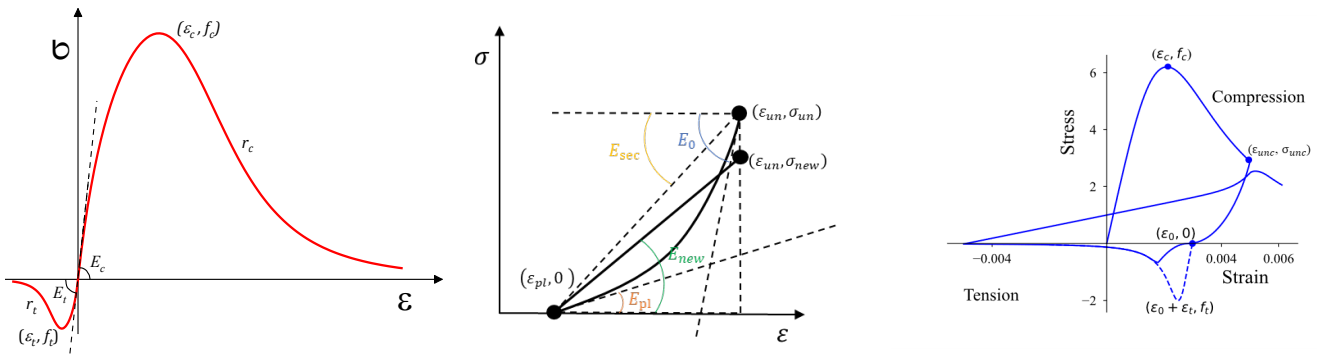

a) Skeleton curve b) Unload and reload curve c) Full curve

Figure 8. ConcreteCM model

For fiber-reinforced concrete, fiber contents have a significant influence on the residual strain, e.g. different volume fractions or aspect ratios of fibers will lead to different residual strains. To properly consider this effect, the ConcreteCM model (seen in Figure 8c) is modified by introducing Eqs. (4) from Li [59,60] in the calculation of the residual strains.

Compression

$$\varepsilon_{plc} = 0.6 \times ulc\left(\frac{\varepsilon_{unc}}{\varepsilon_c}\right)^{1.276} \times \varepsilon_c \qquad E_{sec} = \frac{\sigma_{unc}}{\varepsilon_{unc} - \varepsilon_{plc}}$$

Tension

$$\varepsilon_{plt} = (\varepsilon_{unt} + ult \times 10^{-4}) \times \varepsilon_t \qquad E_{sec} = \frac{\sigma_{unt}}{\varepsilon_{unt} - \varepsilon_{plt}} \tag{4}$$

In Eqs. (4), the residual strain ε_{plc} for compression and ε_{plt} for tension are calculated by the unloading strain ε_{unc} (Seen in Figure 8) for compression and ε_{unt} for tension, respectively. *ulc* and *ult* are two parameters that vary with the mixture of FRC, thus, the residual plastic strain is now mixture-dependent. As a result, in the modified ConcreteCM, there are a total of 10 parameters to be determined, including ε_c, f_c, E_c, r, ulc for compression, and ε_t, f_t, E_t, r_t, ult for tension. Amongst the 10 parameters, *ult* and *ulc* determine the residual strain (ε_{plt}, ε_{plc}), while the remaining parameters define the skeleton curve.

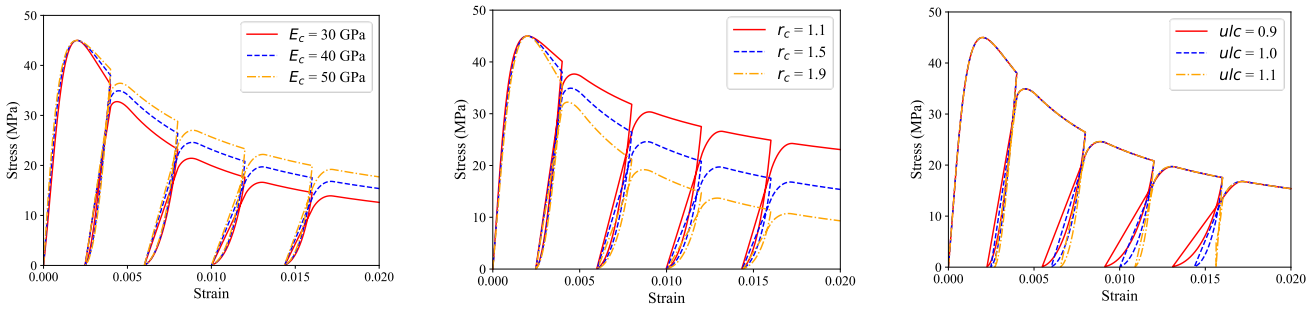

a) E_c b) r_c c) ulc

Figure 9. The effects of the parameters of the modified ConcreteCM

To investigate the influence of the parameters on the curve, a comparison between different values of parameters is carried out for compression. The peak strain and peak stress are set to be 2000 με and 45 MPa, respectively. Figure 9 shows the effect of E_c, r_c, and ulc on the curve of the modified ConcreteCM, where it can be seen that E_c and r_c both affect the descending branch of the curve. The parameter ulc affects the residual strain of the curve and has no effect on the skeleton curve. For the sake of convenience, in the remainder of the paper, r_c and r_t are called skeleton factors, and ulc and ult are named unloading and reloading factors.

3.2.2. Parameter calibration

The purpose of parameter calibration is to find optimal parameters for a physical model to produce results that are close to experimental data. The physical model used here is the modified ConcreteCM proposed in 3.2.1. The 10 parameters to be determined include peak points (f_c, ε_c) and (f_t, ε_t), initial elastic moduli E_c and E_t, skeleton factors r_c and r_t, reloading and unloading factors ult and ulc. The calibration of peak stress and peak strain is relatively simple by directly taking their respective maximum values from the stress-strain curves obtained from experiments. However, the calibration of other parameters is far more complex, hence, a multi-variable optimization process is required.

Using optimization algorithms for multi-variable optimization directly often results in a local minimum and fails to obtain satisfactory results. For the parameters of the modified ConcreteCM, every parameter has its specific effect on the curve, as shown in Figure 9. To best estimate these effects, a method is proposed here to evaluate the parameters in a desirable sequence.

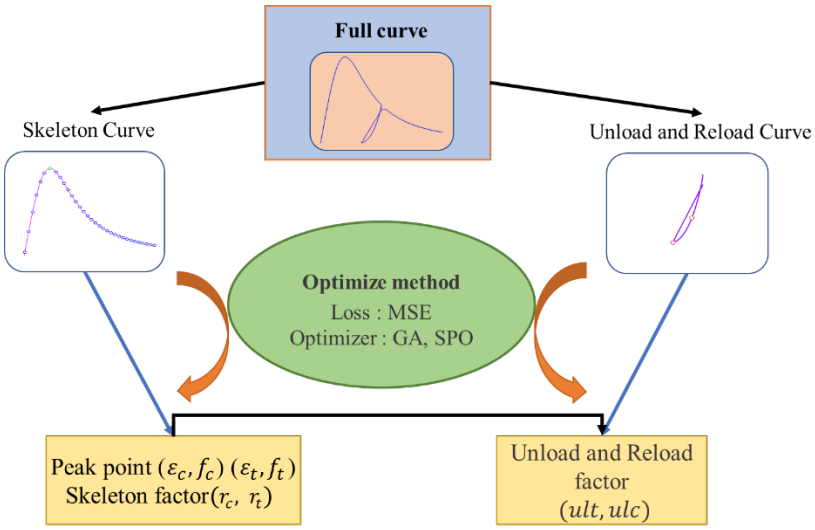

Figure 10. Strategy for parameter calibration

As shown in Figure 10, the initial elastic modulus $E_c(E_t)$ and the skeleton factor $r_c(r_t)$ affect the shape of the skeleton curve but have no effect on the residual strain, and the shape of the skeleton curve is more sensitive to the latter. To decouple these two parameters in the process of calibration, as proposed by Yassin [61], the initial elastic modulus $E_c(E_t)$ takes twice the slope of the secant line at the peak point. For the calibration of skeleton factor $r_c(r_t)$, the mean square error (MSE) between the predict skeleton stress and the skeleton stress from experiments is selected as the loss to find optimal $r_c(r_t)$ value by swam intelligent optimization algorithms. For ulc and ult, since they only affect the residual strain, the MSE of the two special points (the reloading point and the mid-point between the unloading and reloading points) of the experiment curve and the predicted curve is taken as the loss. The same optimization algorithms are used to obtain optimal results. To obtain accurate values of the parameters, two different swam intelligent optimization algorithms, i.e., the gent genetic algorithm (GA) and the particle swimming optimization algorithm (PSO), are used. The results show that the calibrated parameters obtained from both algorithms are almost the same, indicating that the calibrated parameters are satisfactory.

3.3. Neural network for predicting physical model parameters

With the calibrated physical model parameters, a data-driven model that can predict physical model parameters from concrete mixture is developed by a fully connected neural network.

3.3.1. Development of the neural network model utilized

A fully connected neural network[62] consists of an input layer, hidden layers, and an output layer, as shown in Figure 11. The input layer is for data inputting. After linear transformation and activation, the data is delivered to the hidden layers. Similarly, with further linear transformations and activations, the hidden layers process the delivered data from the input layer and pass them to the output layer for the final predictions. For fiber-reinforced concrete, five properties of a concrete mixture, i.e., water to cement ratio, steel fiber volume fraction, steel fiber aspect ratio, polypropylene fiber volume fraction, and polypropylene fiber aspect ratio, are selected as the inputs of the neural network. Peak points,(f_c, ε_c) and (f_t, ε_t), skeleton factors, r_c and r_t, and unloading and reloading factors, ult and ult, are the outputs of neural networks.

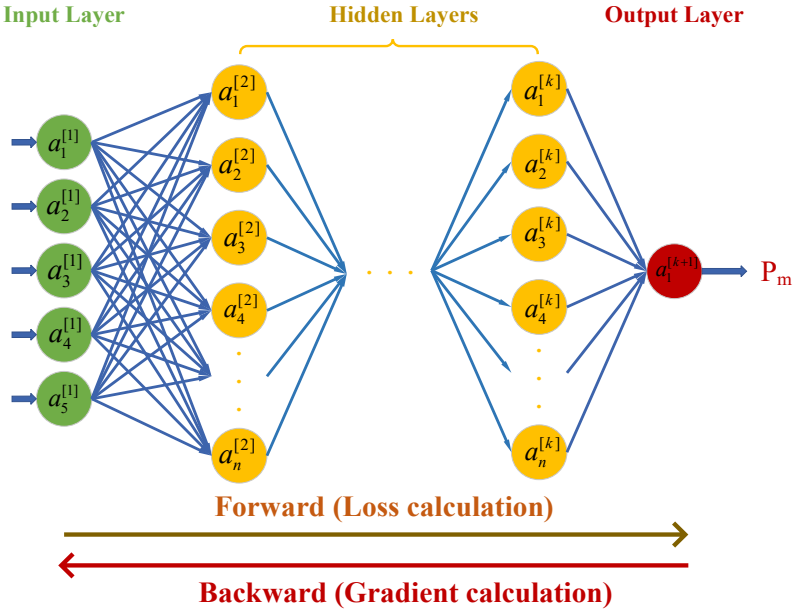

Figure 11. Full connected neural network

Loss:
$$\mathrm{MSE} = \frac{1}{n}\sum_{\mathrm{n}}\left(P_m - P_{exp}\right)^2 \tag{5}$$

Forward:
$$a^{[l]} = f^{[l]}(w^{[l]}a^{[l-1]} + b^{[l]}) \tag{6}$$

Backward:
$$\frac{\partial a^{[l]}}{\partial w^{[l]}} = f^{[l]'}a^{[l-1]}, \quad \frac{\partial a^{[l]}}{\partial b^{[l]}} = f^{[l]'} \tag{7}$$

Optimize:
$$w^{[l]} = w^{[l]} - \alpha\left(\frac{\partial Loss}{\partial w^{[l]}} + \lambda w^{[l]}\right), \quad b^{[l]} = b^{[l]} - \alpha\frac{\partial Loss}{\partial b^{[l]}} \tag{8}$$

Eq. (6) shows the operation on data for every neuron in the network. In this equation, $a^{[l-1]}$ and $a^{[l]}$ are inputs and outputs of the neurons in layer l. $w^{[l]}$ and $b^{[l]}$ are weight and bias of the network and need to be trained first. $f^{[l]}$ is an activation function that are normally nonlinear. Mean square error (MSE) is select as the loss of the neural network, seen in Eq. (5). The neuron network is trained by the backpropagation (BP) algorithm[63], where the gradient of the weights and bias are calculated by Eq. (7). The weights $w^{[l]}$ and bias $b^{[l]}$ are updated by optimization in Eq. (8). The network utilizes two hyperparameters, denoted as α and λ, which correspond to the learning rate and weight decay, respectively. These hyperparameters determine the training speed and alleviating overfitting of the network. Weight decay, specifically, is a regularization technique employed to mitigate the complexity of neural networks and address overfitting. This technique involves incorporating a regularization term into the loss function, which penalizes larger weight values and promotes a smoother model. Throughout the training process, weight decay encourages the network to prioritize smaller weight values, effectively regulating the model's complexity and enhancing its generalization capability.

To prevent any unwanted coupling effects among the outputs of the neural network in training, networks are built and trained separately for each of the physical model parameters. The number of hidden layers of each independent neural network model is set to be two, and each hidden layers has five neurons. Hyperbolic tangent function (tang) is used as the activation function.

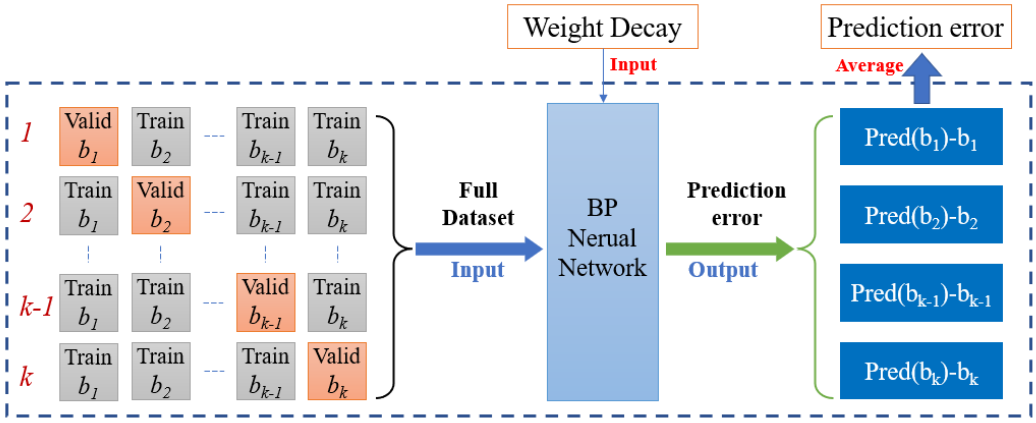

Figure 12. Schema of k-cross validation

The power of neural networks lies in its ability to identify complicated relationships hidden in data. In principal, a larger data set will reduce noises and result in better performance. In this paper, due to a relatively small set of data, A K-fold cross-validation scheme is followed to test the networks, which divides the data evenly into k subsets, each of which is tested while other subsets serve as training sets. By evaluating the overall performance of the neural network, the hyper-parameters of the neural network can be determined (Figure 12). The same architecture, i.e., five neurons in the input layer, two hidden layers with five neurons each, and one neuron in the output layer, is set for all the eight neural networks trained in this study. L2 regularization method[64] is used to alleviate overfitting of the networks. The values of weight decay are determined for each of the neural networks by the k-fold cross validation method.

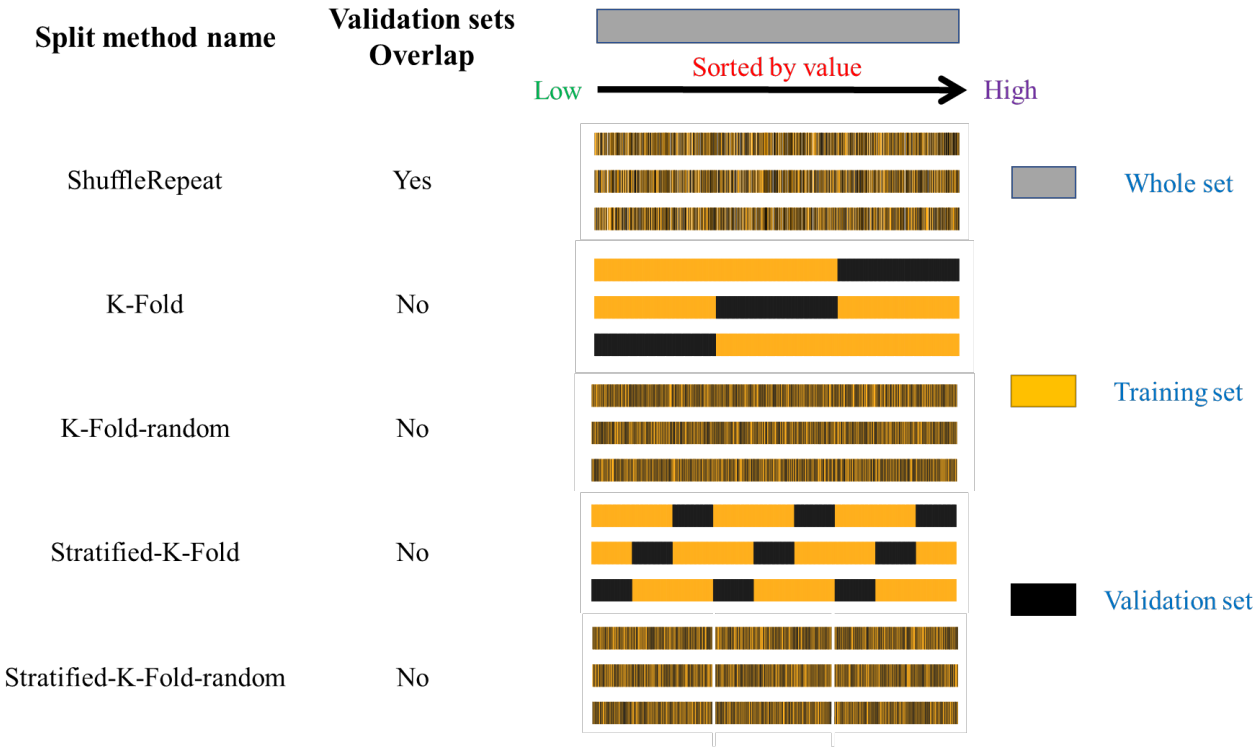

Figure 13. Different methods to divide training set and validation set

Five validation methods are compared, including Shuffle repeat, K-Fold, K-Fold-random[65–67], Stratified-K-Fold and Stratified-K-Fold-random[68–71], as shown in Figure 13 where k is 3. The dataset is first sorted in an ascending order of the output, e.g. from the highest to the lowest experimental peak stresses. This applies to all the eight outputs before they are trained and tested using the above 5 K-fold validation approaches.

3.3.2. Comparison of different k-cross validation methods

As mentioned in Section 3.3.1, 8 BP neural networks are built and trained with different validation methods. Figure 14 shows the mean percentage error of the networks in predicting the eight parameters for various weight decays. In Figure 14, the solid curves are the results of the training set and the dotted curves are the results of the validation set, respectively. As the weight decay increases, the mean percentage error of the training set rises gradually. For the validation set, the mean percentage error decreases first before it starts increasing, indicating that the neural networks change from under-fitting to over-fitting. For the nonrandom dividing method (K-fold and Stratified-k-fold), the mean percentage error of the validation set is bigger because the range of the training and the validation sets are more likely to be exclusive to each other. Among the three random sampling approaches, the Stratified k-fold random method outperforms others (shown in Figure 14). It may be attributed to the distribution of the validations set that is within the distribution range of the training set. On the basis of the comparisons, the Stratified k-fold random method is chosen in this study to find the best weight decay value to reduce overfitting of the neural networks.

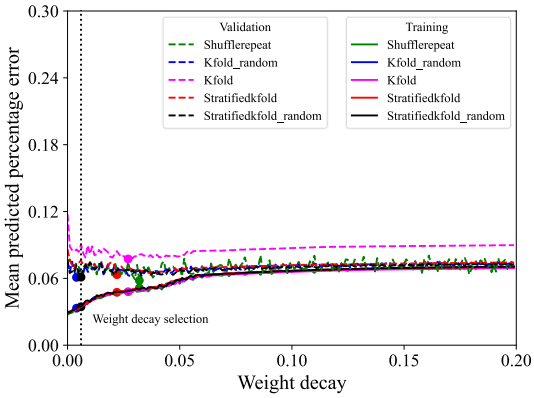

a) compressive peak stress f_c

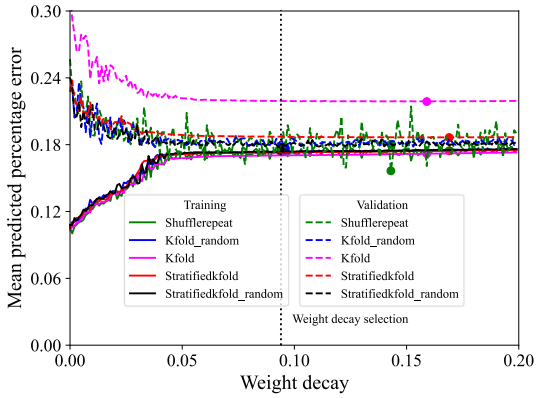

b) compressive peak strain ε_c

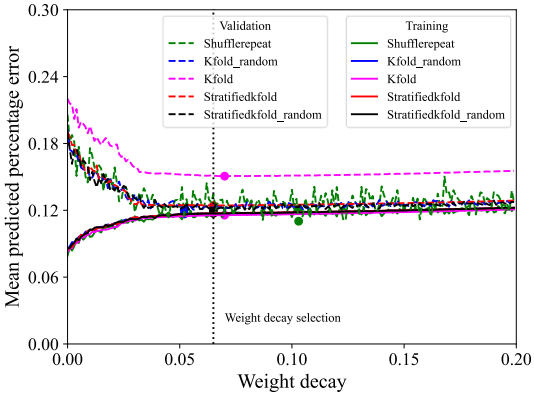

c) compressive r_c

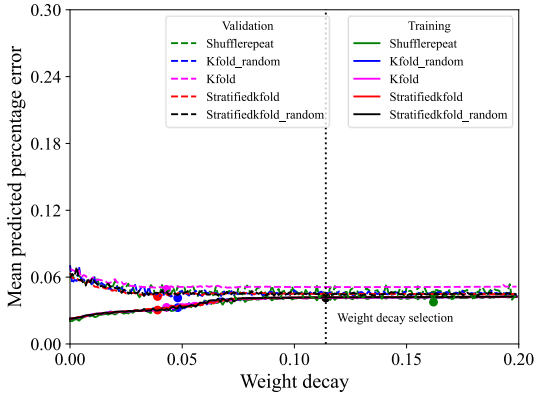

d) compressive ulc

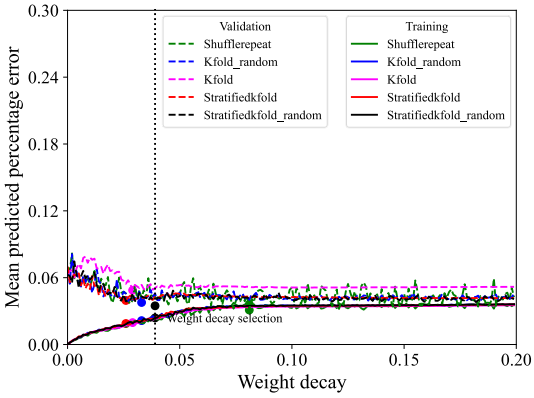

e) tensile peak stress f_t

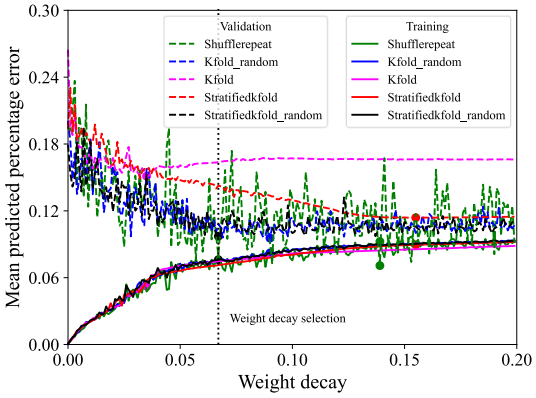

f) tensile peak strain ε_t

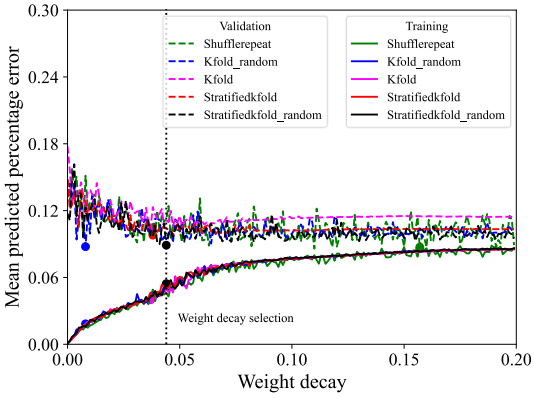

g) tensile r_t

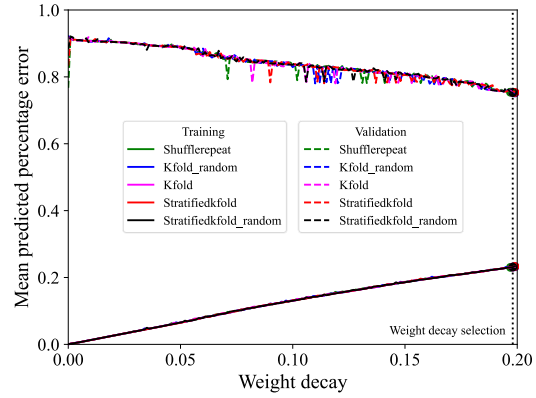

h) tensile ult

Figure 14. Selection of weight decay in k-cross validation

The mean percentage error of the network for peak stresses are under 0.1 for both f_c (Figure 14a) and f_t (Figure 14e) of the validation set, suggesting a good performance of the networks. For compressive peak strain ε_c and tensile peak strain ε_t, the errors of the validation set is bigger than 0.10. For the skeleton factors, r_c and r_t, the error is around 0.1. For the tensile ult, the mean percentage error of the prediction is very high, which is caused by a lack of tensile specimens. The error of the network for ulc is very small and is almost constantly around 0.05. Overall, it has been demonstrated that most of the trained networks are sufficiently accurate.

The L2 regularization (weight decay) value is determined when he mean percentage error of the validation set is minimum. For the eight BP neural networks of peak compressive strain, peak compressive stress, compressive skeleton factor, compressive load/unload factor, peak tensile strain, peak tensile stress, tensile skeleton factor, and tensile load/unload factor, the weight decays are 0.094, 0.006, 0.065, 0.114, 0.067, 0.039, 0.044 and 0.198, respectively, as shown by the dashed vertical lines in Figure 14).

4. Evaluation of the physics-based data-driven model

In this section, evaluation, and discussion of the parameter calibration, neural network, and uniaxial constitute model established by the physics-based data-driven framework are presented. Mean absolute error (MAE), root mean square error (RMSE), correlation coefficient (r), and index of confidence (p) are calculated (Eq.11-14) and used as the evaluation criteria[72,73].

$$MAE = N^{-1}\sum_{i=1}^{N}|P_i - O_i| \tag{11}$$

$$RMSE = \sqrt{N^{-1}\sum_{i=1}^{N}(P_i - O_i)^2} \tag{12}$$

$$r = \frac{\sum_{i=1}^{N}(P_i - \overline{P})(O_i - \overline{O})}{\sqrt{\sum_{i=1}^{N}(P_i - \overline{P})^2}\sqrt{\sum_{i=1}^{N}(O_i - \overline{O})^2}} \tag{13}$$

$$p = \left(1 - \frac{\sum_{i-1}^{N}(P_i - O_i)^2}{\sum_{i=1}^{N}(|P_i - O| + |O_i - O|)^2}\right) \times r \tag{14}$$

In Eqs. 11-14, P is the model predicted value and O is the observed value of the experiments. The performance of the model is assessed based on the value of p, as shown in Table 2.

Table 2. Classification of confident index[73]

Performance:	Great	Very good	Good	Average	Tolerable	Bad	Very bad
p-Value:	≥0.85	0.75-0.85	0.65-0.75	0.60-0.65	0.50-0.60	0.40-0.50	≤0.40

4.1. Evaluation of parameter calibration

Parameter calibration is the first step of the proposed framework, which calibrates critical physical model parameters from experimental data by swarm intelligent optimization algorithms. Using the calibrated physical model parameters and the measured strains from experiments, the stresses are predicted and compared with the stresses from experiments by calculating MAE, RMSE, r, and p. The results are shown in Figure 15 and Figure 16.

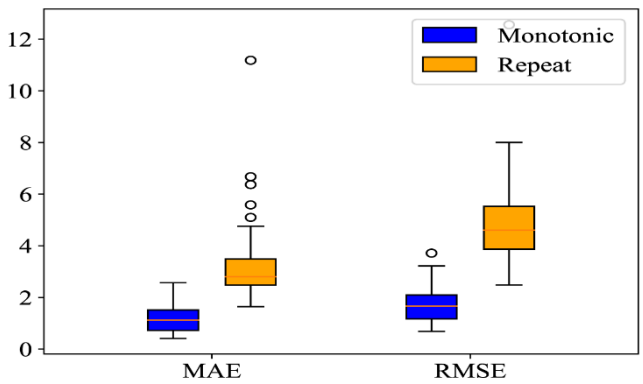

a) Distribution of MAE and RMSE

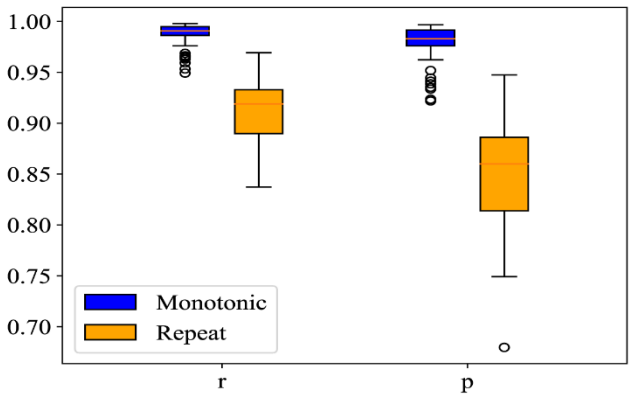

b) Distribution of r and p

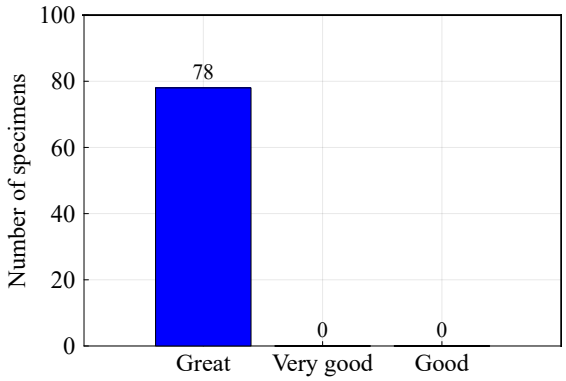

c) Performance of calibrated parameters for monotonic experiments

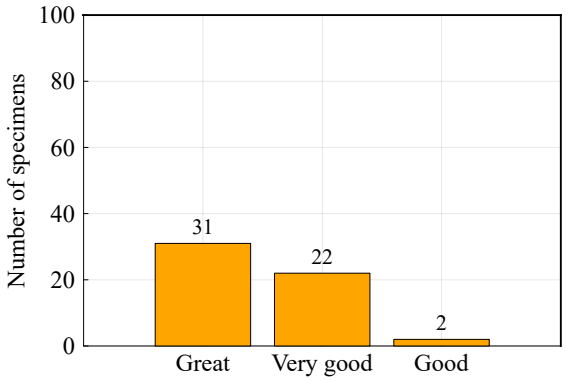

d) Performance of calibrated parameters for repeat experiments

Figure 15. Evaluation of parameters calibration on compressive experiments

Figure 15 shows the evaluation for compression. The MAE and RMSE of all the samples subjected to monotonic compression are smaller than 4, indicating that the physical model is sufficiently accurate for monotonic compression. For the specimens subjected to repeated loads, both MAE and RMSE are increased. However, the MAE and RMSE of 90% of the specimens remain below 6. The correlation coefficients (r) for all the specimens are greater than 0.8. The distribution of index of confidence (p) shows that the p-value of 90% of samples is also bigger than 0.8 (Figure 15b). The classification of the prediction of the physical model is shown in Figure 15(c) and Figure 15(d). All the samples subjected to monotonic loading and more than 50% of the samples subjected to repeated loading are classified as "Great", where only 2 samples in Figure 15(d) are downgraded to "good" while the others are "Very good" when they are classified using the specification defined in Table 2.

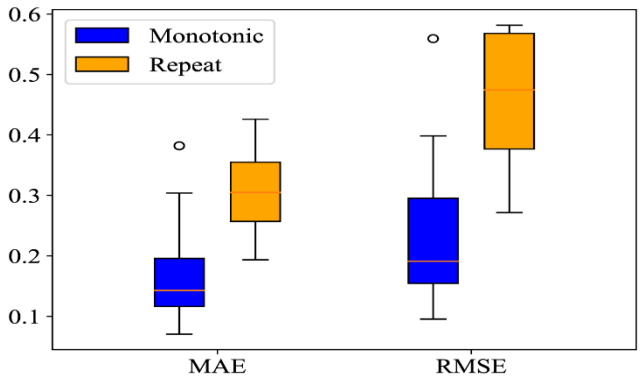

a) Distribution of MAE and RMSE

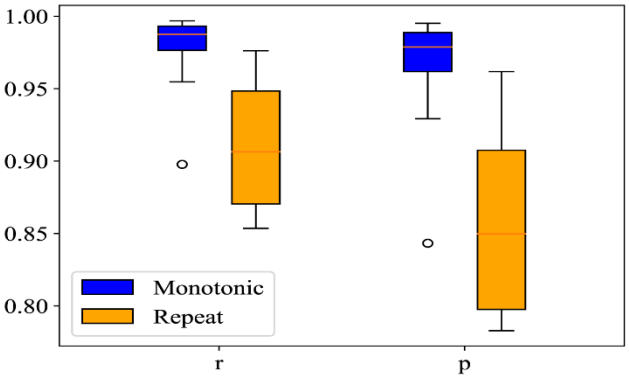

b) Distribution of r and p

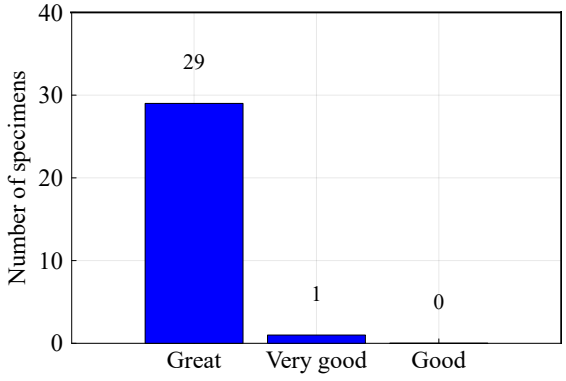

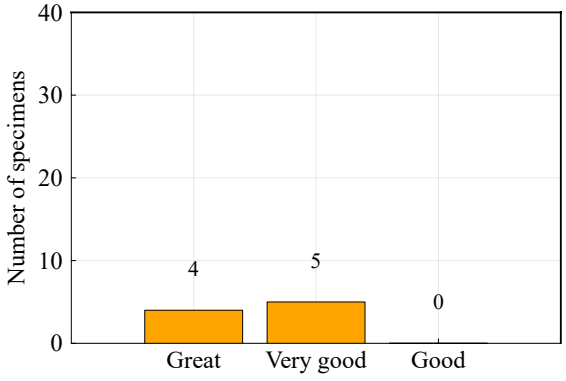

c) Performance of calibrated parameters monotonic experiments

d) Performance of calibrated parameters repeat experiments

Figure 16. Evaluation of parameters calibration on tensile experiments

For the samples subjected to tension, because the stresses are low, smaller MAE and RMSE are calculated compared to the compressive samples. Similar to the observations from the compressive samples, the specimens subjected to monotonic loading show better comparisons than the specimens subjected to repeated loading, due to the simpler load pattern. The correlation coefficients (r) of all the samples are greater than 0.85. The classification of the predictions from the trained physical models are shown in Figure 16(c) and Figure 16(d). For all the specimens subjected to monotonic tension, the confidence indexes are classified as "Great" except one specimen that is classified as "Very good". For the specimens subjected to repeated tension, all the 9 specimens are classified at least as "Very good". Overall, 33 specimens are classified as "Great", accounting for 84.6% of the total samples in tension. The rest of the specimens are classified at least as "Very good", showing that the modified physical model is capable of predicting satisfactorily the mechanical behavior of fiber-reinforced concrete under tensile loads.

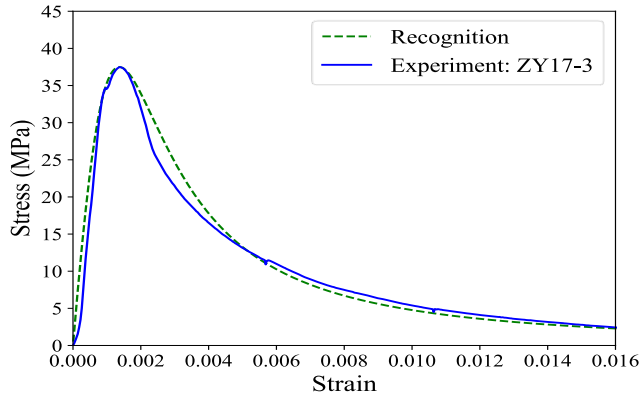

a) Monotonic compressive experiment

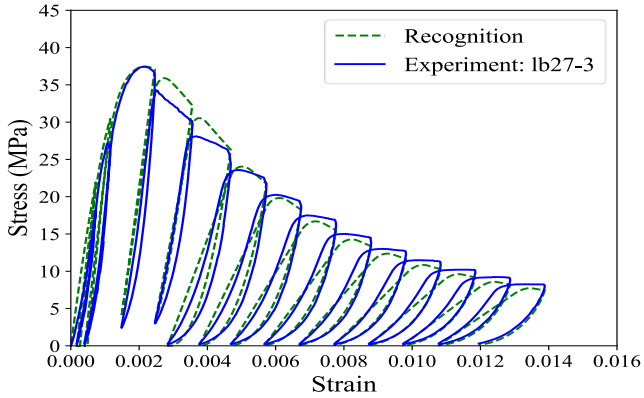

b) Repeat compressive experiment

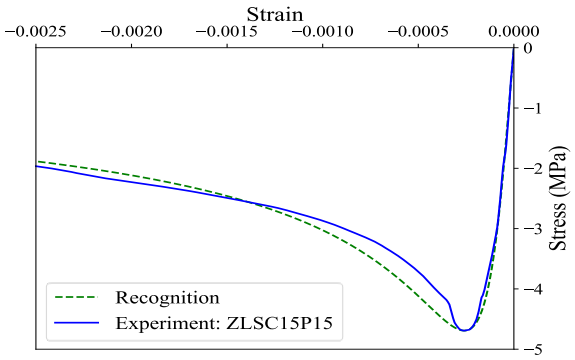

c) Monotonic tensile experiment

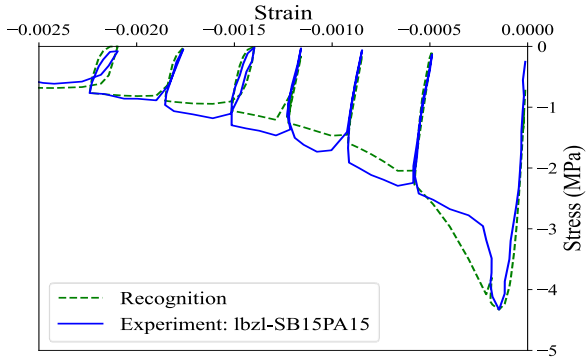

d) Repeat tensile experiment

Figure 17. Stress-strain curve of the modified model with optimized parameters

In Figure 17, the stress-strain curves predicted by the modified physical model with calibrated parameters are compared with the experimental stress-strain curves for samples under various loading patterns, where positive strains and stresses are for compression and negative for tension, respectively. It is evident that the predicted curves are close to the experimental ones.

4.2. Evaluation of proposed neural network

Fully connected neural networks are designed and trained to find the physical model parameters of given mixtures.

In the training process, k-cross validation and L2 regularization methods are used to alleviate overfitting of the network. The final predictions of the neural networks are compared with the calibrated physical model parameters (Target), which are shown in Figure 18 below.

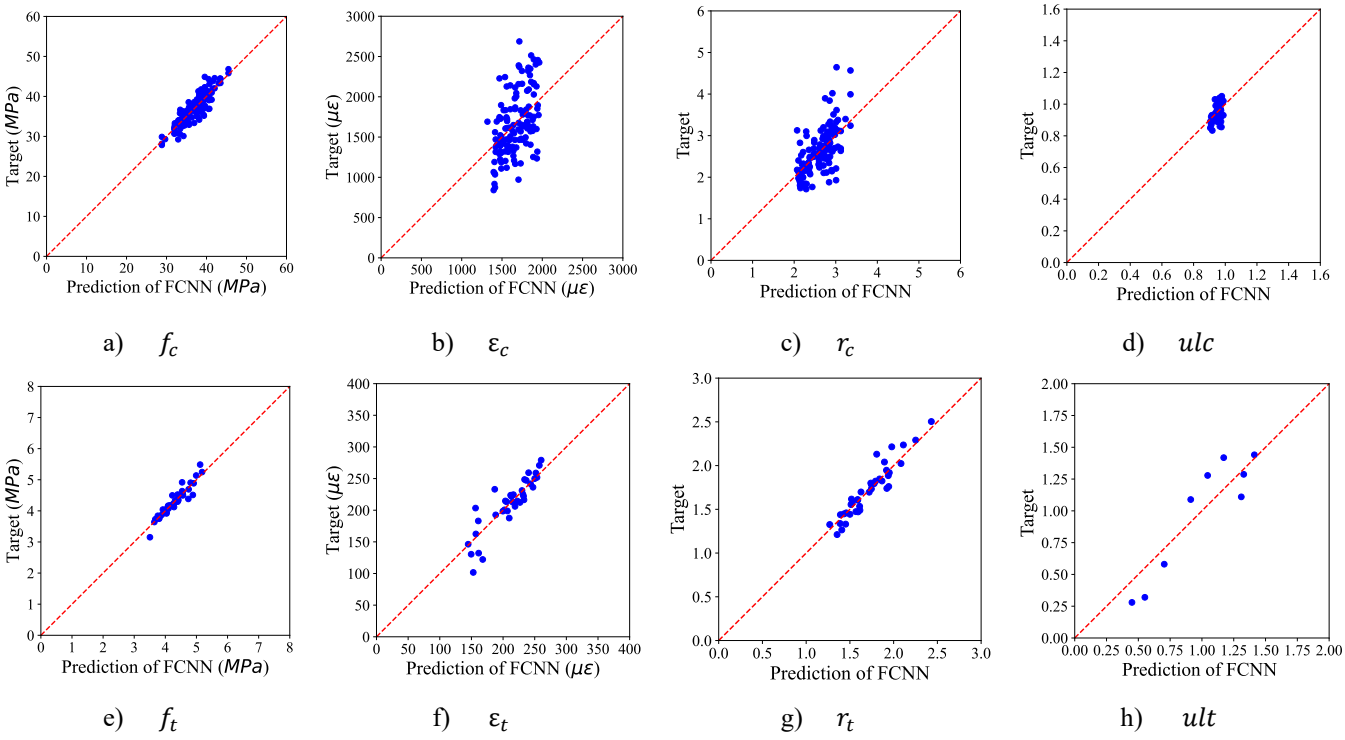

Figure 18. Prediction of the trained neural network

Eight fully connected neural networks are trained using the weight decays determined in Section 3.3.2. For predicting compressive peak stress, tensile peak stress, tensile peak strain, skeleton factor r_t and r_c , five of the networks show excellent performance. For compressive peak strain, and compressive ulc, the predictions of these two networks are not very good, indicating underfitting has occurred, suggesting that deeper networks may be required for better predictions. For the tensile ult, overfitting occurs in the network due to the small size of the data set. The results are consistent with the analysis using the k-cross validation methods in Section 3.3.2. Overall, most of the network can give acceptable predictions on the parameters of the modified physical model.

4.3. Validation of the model with test results

For a given mixture, the physical model parameters can be predicted by the trained neural networks, hence, the strain path and stresses of the concrete can be further predicted the modified physical model. Figure 19 and Figure 20 show the MAE, RMSE, r, and p calculated for the comparison between the predicted stresses and those from the experiments.

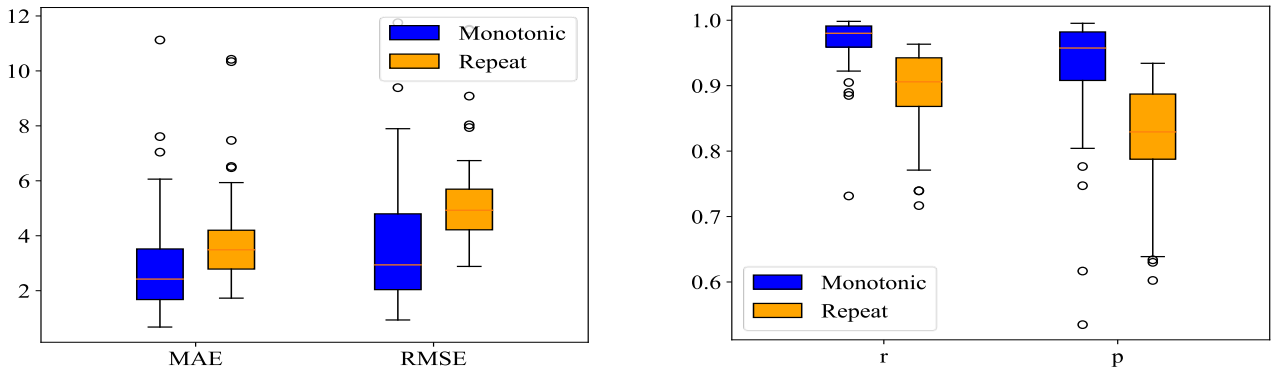

a) Distribution of MAE and RMSE

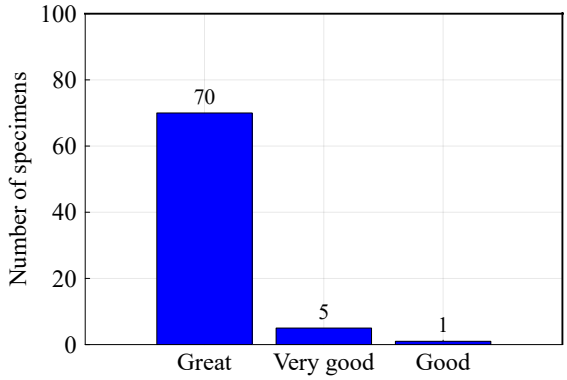

b) Distribution of r and p

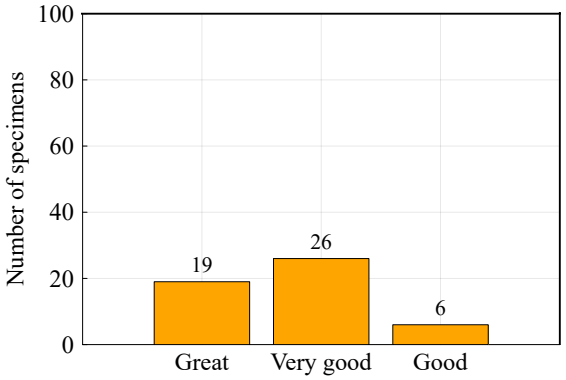

c) Performance of proposed model for monotone experiments

d) Performance of proposed model for repeat experiments

Figure 19. Evaluation of the final model on compressive experiments

For the samples subjected to compression, the MAE and RMSE rise slightly compared to the results shown in Figure 15. For 90% of the samples, the MAE and RMSE are less than 8, with also slightly reduced correlation coefficient (r). For the performance classification, the number of monotonic samples that are classified as “Great” decreases by 8, and most of the samples in the group of repeated loading are downgraded from “Great” to “Very good”. The reason for the declined performance is attributed to the prediction error of the neural networks.

For the tensile samples, as shown in Figure 20, the MAE and RMSE are small. The distribution of correlation coefficient (r) almost stays the same compared to Figure 16(b). The classification of performance remains virtually unchanged compared to Figure 16(c) and Figure 16(d).

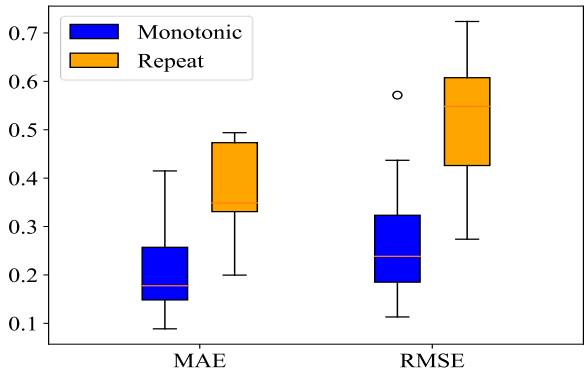

a) Distribution of MAE and RMSE

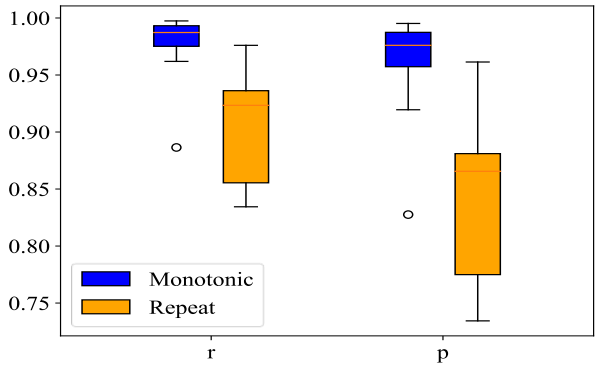

b) Distribution of r and p

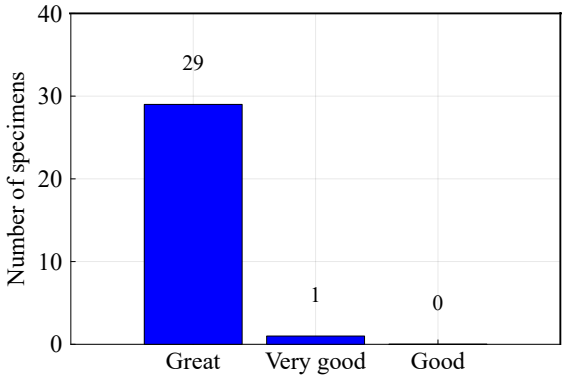

c) Performance of network for monotonic experiments

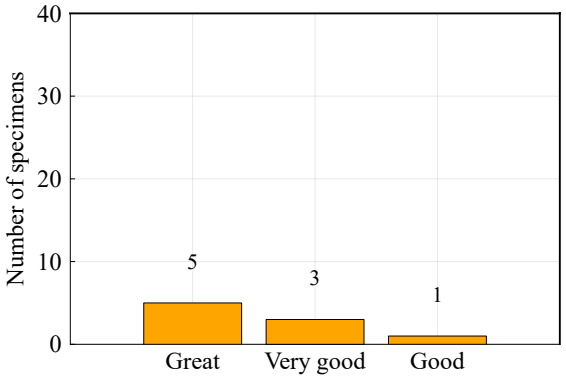

d) Performance of network for repeated experiments

Figure 20. Evaluation of the final model on tensile experiments

Figure 21 shows the predicted curves and the averages of the curves from experiments for different load patterns. It can be seen that the predicted curves agree with the curves from experiments reasonably well. It is expected that the prediction would be more accurate when more data are available in the training process. The label behind experiment, for example ZY17-1 in Figure 21a), represents the label of specific experiment in the database.

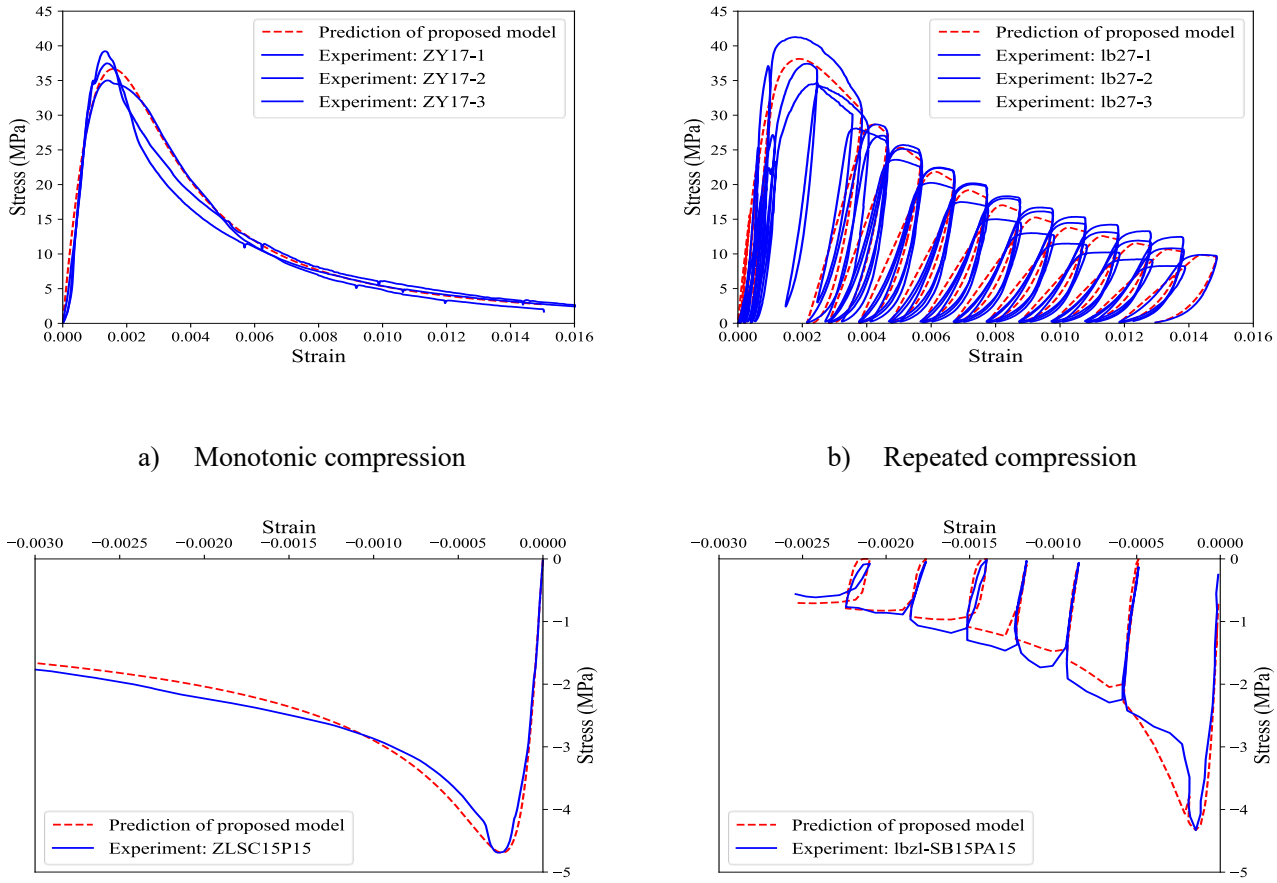

a) Monotonic compression

b) Repeated compression

c) Monotonic tension

d) Repeat tension

Figure 21. Prediction of the modified model for fiber-reinforced concrete under different load patterns

5. Conclusion

A physics-based data-driven framework has been developed in this paper for accurate prediction of mechanical properties of fiber reinforced concrete subjected to compression, tension and repeated loading. The modified ConcreteCM model was chosen as the basic physics model that, along with the experimental data, participated in training process of the neural network. The training process was to learn some of the most critical material parameters that are essential in defining the stress-strain relationships of the FRC. The learned parameters were used then to establish the constitutive law for FRC with consideration of its fiber content and concrete composition. The main contributions and conclusions of this study are summarized as follows.

1. **Development of a database with a user-friendly interface**: To support the framework, a database of experimental test results was developed with a friendly graphical user interface. The database, which was created using the data collected from the literature, offers functionalities such as data import, modification, export, statistical analysis, classification and visualization. The database is open-ended and any future data may be added to the system.

2. **Development of a physics-based data-driven framework**: This study introduced a novel framework that combines physics-based models with data-driven methods. This framework has the potential to take full advantages of

both the definitive physics modelling and the diverse but more practically informative experimental data, which can provide more accurate, reliable and robust predictions to the mechanical behavior of fiber-reinforced concrete under uniaxial loading.

3. **Modification of the ConcreteCM model**: Informed by the experimental data through machine learning, modifications were made to the existing ConcreteCM model, making it more suitable for fiber-reinforced concrete. This was done by calculating residual plastic strain from concrete mixture rather than the macroscale properties of a concrete thorough the introduction of two additional parameters to ConcreteCM, along with the concrete mixture, in the data training process.

4. **Assessment of neural network performance**: The performance of the neural networks used in the framework was assessed using various validation methods. It was found that a randomized approach produced lower but unstable final loss values. However, by implementing a well-designed validation method, such as Stratifiedkfold, the performance of the neural networks was significantly improved.

5. **Potential for broader applications**: The application of the developed framework is not limited to fiber-reinforced concrete. The proposed physics-based data-driven framework has the potential to be applied to other physical problems that benefits from the integration of physical models and experimental data. This opens up new possibilities for solving complex engineering problems by combining the strengths of physics-based models and data-driven approaches.

Research significance

Inspired by the explosive growth of artificial intelligence (AI) methods in civil engineering applications, and the rise of data-centric computing, which is forming the foundation for a digital economy and society, this study presents a novel framework that combines physics-based models with data-driven methods. The application of the framework to the development of the uniaxial constitutive model for fiber-reinforced concrete makes it advantageous in considering the effect of fibre contents and concrete mixture of each individual FRC. The user-friendly interface and the adaptability of the framework, make it a useful tool in assessing material properties of FRC and design of structures using FRC components when it interacts with other design and analysis software. The framework can be easily extended to other engineering fields.

Data availability

The raw/processed data required to reproduce these findings cannot be shared at this time due to technical or time limitations.

Declaration of Competing Interest

The authors declare that they have no known competing financial interests or personal relationships that could have appeared to influence the work reported in this paper.

Acknowledgments

This work was supported by the National Natural Science Foundation of China (Grant Nos. 52178157, 51978538).

Reference

[1] X. Wei, M. Ren, P. Feng, X. Wu, J. Liao, A Review and Prospect for Fracture Properties of Fiber-Reinforced Concrete, Industrial Construction. 52 (2022) 1–9. https://doi.org/10.13204/j.gyjzG20102205.

[2] H. Chen, P. Hou, X. Zhou, L. Black, S. Adu-Amankwah, P. Feng, N. Cui, M.A. Glinicki, Y. Cai, S. Zhang, P. Zhao, Q. Li, X. Cheng, Toward performance improvement of supersulfated cement by nano silica: Asynchronous regulation on the hydration kinetics of silicate and aluminate, Cement and Concrete Research. 167 (2023). https://doi.org/10.1016/j.cemconres.2023.107117.

[3] M. Zajac, J. Skocek, S. Adu-Amankwah, L. Black, M. Ben Haha, Impact of microstructure on the performance of composite cements: Why higher total porosity can result in higher strength, Cement and Concrete Composites. 90 (2018) 178–192. https://doi.org/10.1016/j.cemconcomp.2018.03.023.

[4] F. Xu, Study on Uniaxial Tensile Behavior and Stress-strain Relationship of Ultra-high performance Concrete with Coarse Aggregate, Wuhan University, 2022.

[5] M. Bhogone, K.V.L. Subramaniam, Early-age tensile constitutive relationships for steel and polypropylene fiber reinforced concrete, Eng. Fract. Mech. 244 (2021). https://www.webofscience.com/wos/alldb/full-record/WOS:000695478700008 (accessed July 16, 2023).

[6] N. Kachouh, T. El-Maaddawy, H. El-Hassan, B. El-Ariss, Shear Response of Recycled Aggregates Concrete Deep Beams Containing Steel Fibers and Web Openings, Sustainability. 14 (2022) 945. https://doi.org/10.3390/su14020945.

[7] A.F. Deifalla, A.G. Zapris, C.E. Chalioris, Multivariable Regression Strength Model for Steel Fiber-Reinforced Concrete Beams under Torsion, Materials. 14 (2021) 3889. https://doi.org/10.3390/ma14143889.

[8] C.E. Chalioris, T.A. Panagiotopoulos, Flexural analysis of steel fibre-reinforced concrete members, Comput. Concr. 22 (2018) 11–25. https://doi.org/10.12989/cac.2018.22.1.011.

[9] C. Ding, D. Gao, A. Guo, Analytical methods for stress-crack width relationship and residual flexural strengths of 3D/4D/5D steel fiber reinforced concrete, Constr. Build. Mater. 346 (2022) 128438. https://doi.org/10.1016/j.conbuildmat.2022.128438.

[10] Silvia Mazzoni, Frank McKenna, Michael H. Scott, Gregory L.Fenves, OpenSees Command Language Manual, (2006). https://opensees.berkeley.edu/wiki/index.php/UniaxialMaterial_Command.

[11] D. Gao, Stress-strain curves of steel fibre concrete under axial compression, SHUILI XUEBAO. (1991) 43–48.

[12] Z. Guo, X. Zhang, D. Zhang, R. Wang, Experimental Investigation of the Complete Stress-Strain Curve of Concrete, Journal of Building Structures. (1982) 1–12. https://doi.org/10.14006/j.jzjgxb.1982.01.001.

[13] B. Li, Elastoplastic Damage Constitutive Model of Steel-Polypropylene Hybrid Fiber Reinforced Concrete and Its Numerical Implementation, Ph.D, Wuhan University, 2018.

[14] M.M. Moein, A. Saradar, K. Rahmati, S.H.G. Mousavinejad, J. Bristow, V. Aramali, M. Karakouzian, Predictive models for concrete properties using machine learning and deep learning approaches: A review, J. Build. Eng. 63 (2023) 105444. https://doi.org/10.1016/j.jobe.2022.105444.

[15] J.-S. Chou, C.-K. Chiu, M. Farfoura, I. Al-Taharwa, Optimizing the Prediction Accuracy of Concrete Compressive Strength Based on a Comparison of Data-Mining Techniques, Journal of Computing in Civil Engineering. 25 (2011) 242–253. https://doi.org/10.1061/(ASCE)CP.1943-5487.0000088.

[16] B.A. Omran, Q. Chen, R. Jin, Comparison of Data Mining Techniques for Predicting Compressive Strength of Environmentally Friendly Concrete, Journal of Computing in Civil Engineering. 30 (2016) 04016029. https://doi.org/10.1061/(ASCE)CP.1943-5487.0000596.

[17] H. Tanyildizi, Prediction of the Strength Properties of Carbon Fiber-Reinforced Lightweight Concrete Exposed to the High Temperature Using Artificial Neural Network and Support Vector Machine, Advances in Civil

Engineering. 2018 (2018) e5140610. https://doi.org/10.1155/2018/5140610.

[18] A.L. Bonifácio, J.C. Mendes, M.C.R. Farage, F.S. Barbosa, C.B. Barbosa, A.-L. Beaucour, Application of Support Vector Machine and Finite Element Method to predict the mechanical properties of concrete, Lat. Am. j. Solids Struct. 16 (2019) e205. https://doi.org/10.1590/1679-78255297.

[19] P.R. Prem, A. Thirumalaiselvi, M. Verma, Applied linear and nonlinear statistical models for evaluating strength of Geopolymer concrete, Computers and Concrete. 24 (2019) 7–17. https://doi.org/10.12989/cac.2019.24.1.007.

[20] Y. Ayaz, A.F. Kocamaz, M.B. Karakoç, Modeling of compressive strength and UPV of high-volume mineral-admixtured concrete using rule-based M5 rule and tree model M5P classifiers, Construction and Building Materials. 94 (2015) 235–240. https://doi.org/10.1016/j.conbuildmat.2015.06.029.

[21] A. Behnood, J. Olek, M.A. Glinicki, Predicting modulus elasticity of recycled aggregate concrete using M5′ model tree algorithm, Construction and Building Materials. 94 (2015) 137–147. https://doi.org/10.1016/j.conbuildmat.2015.06.055.

[22] M.-Y. Cheng, P.M. Firdausi, D. Prayogo, High-performance concrete compressive strength prediction using Genetic Weighted Pyramid Operation Tree (GWPOT), Engineering Applications of Artificial Intelligence. 29 (2014) 104–113. https://doi.org/10.1016/j.engappai.2013.11.014.

[23] A.T.A. Dantas, M. Batista Leite, K. de Jesus Nagahama, Prediction of compressive strength of concrete containing construction and demolition waste using artificial neural networks, Construction and Building Materials. 38 (2013) 717–722. https://doi.org/10.1016/j.conbuildmat.2012.09.026.

[24] C. Deepa, K. SathiyaKumari, V.P. Sudha, Prediction of the Compressive Strength of High Performance Concrete Mix using Tree Based Modeling, IJCA. 6 (2010) 18–24. https://doi.org/10.5120/1076-1406.

[25] F. Deng, Y. He, S. Zhou, Y. Yu, H. Cheng, X. Wu, Compressive strength prediction of recycled concrete based on deep learning, Construction and Building Materials. 175 (2018) 562–569. https://doi.org/10.1016/j.conbuildmat.2018.04.169.

[26] A. Gholampour, I. Mansouri, O. Kisi, T. Ozbakkaloglu, Evaluation of mechanical properties of concretes containing coarse recycled concrete aggregates using multivariate adaptive regression splines (MARS), M5 model tree (M5Tree), and least squares support vector regression (LSSVR) models, Neural Comput & Applic. 32 (2020) 295–308. https://doi.org/10.1007/s00521-018-3630-y.

[27] T. Gupta, K.A. Patel, S. Siddique, R.K. Sharma, S. Chaudhary, Prediction of mechanical properties of rubberised concrete exposed to elevated temperature using ANN, Measurement. 147 (2019) 106870. https://doi.org/10.1016/j.measurement.2019.106870.

[28] F. Khademi, M. Akbari, S.M. Jamal, M. Nikoo, Multiple linear regression, artificial neural network, and fuzzy logic prediction of 28 days compressive strength of concrete, Front. Struct. Civ. Eng. 11 (2017) 90–99. https://doi.org/10.1007/s11709-016-0363-9.

[29] H. Naderpour, A.H. Rafiean, P. Fakharian, Compressive strength prediction of environmentally friendly concrete using artificial neural networks, Journal of Building Engineering. 16 (2018) 213–219. https://doi.org/10.1016/j.jobe.2018.01.007.

[30] A. Nazari, J.G. Sanjayan, Modelling of compressive strength of geopolymer paste, mortar and concrete by optimized support vector machine, Ceramics International. 41 (2015) 12164–12177. https://doi.org/10.1016/j.ceramint.2015.06.037.

[31] Z.M. Yaseen, R.C. Deo, A. Hilal, A.M. Abd, L.C. Bueno, S. Salcedo-Sanz, M.L. Nehdi, Predicting compressive strength of lightweight foamed concrete using extreme learning machine model, Advances in Engineering Software. 115 (2018) 112–125. https://doi.org/10.1016/j.advengsoft.2017.09.004.

[32] J. Zhang, G. Ma, Y. Huang, J. sun, F. Aslani, B. Nener, Modelling uniaxial compressive strength of lightweight self-compacting concrete using random forest regression, Construction and Building Materials. 210

(2019) 713–719. https://doi.org/10.1016/j.conbuildmat.2019.03.189.

[33] D. Simon, Biogeography-Based Optimization, IEEE Transactions on Evolutionary Computation. 12 (2008) 702–713. https://doi.org/10.1109/TEVC.2008.919004.

[34] A. Behnood, J. Olek, M.A. Glinicki, Predicting modulus elasticity of recycled aggregate concrete using M5′ model tree algorithm, Construction and Building Materials. 94 (2015) 137–147. https://doi.org/10.1016/j.conbuildmat.2015.06.055.

[35] E.M. Golafshani, A. Behnood, Automatic regression methods for formulation of elastic modulus of recycled aggregate concrete, Applied Soft Computing. 64 (2018) 377–400. https://doi.org/10.1016/j.asoc.2017.12.030.

[36] J. Xu, X. Zhao, Y. Yu, T. Xie, G. Yang, J. Xue, Parametric sensitivity analysis and modelling of mechanical properties of normal- and high-strength recycled aggregate concrete using grey theory, multiple nonlinear regression and artificial neural networks, Construction and Building Materials. 211 (2019) 479–491. https://doi.org/10.1016/j.conbuildmat.2019.03.234.

[37] A. Behnood, K.P. Verian, M. Modiri Gharehveran, Evaluation of the splitting tensile strength in plain and steel fiber-reinforced concrete based on the compressive strength, Construction and Building Materials. 98 (2015) 519–529. https://doi.org/10.1016/j.conbuildmat.2015.08.124.

[38] P.O. Awoyera, M.S. Kirgiz, A. Viloria, D. Ovallos-Gazabon, Estimating strength properties of geopolymer self-compacting concrete using machine learning techniques, Journal of Materials Research and Technology. 9 (2020) 9016–9028. https://doi.org/10.1016/j.jmrt.2020.06.008.

[39] J.-S. Chou, N.-T. Ngo, A.-D. Pham, Shear Strength Prediction in Reinforced Concrete Deep Beams Using Nature-Inspired Metaheuristic Support Vector Regression, Journal of Computing in Civil Engineering. 30 (2016) 04015002. https://doi.org/10.1061/(ASCE)CP.1943-5487.0000466.

[40] Jie Z., Tingting Z., Qingqing C., Zhiyong W., Zhihua W., Prediction of Concrete Meso-Model Stress-Strain Curves Based on GoogLeNet, yysxhlx. 43 (2022) 290–299. https://doi.org/10.21656/1000-0887.420136.

[41] N. Zhang, S.-L. Shen, A. Zhou, Y.-F. Jin, Application of LSTM approach for modelling stress-strain behaviour of soil, Appl. Soft. Comput. 100 (2021) 106959. https://doi.org/10.1016/j.asoc.2020.106959.

[42] G.A. Chang, J.B. Mander, Seismic Energy Based Fatigue Damage Analysis of Bridge Columns: Part 1 - Evaluation of Seismic Capacity, (n.d.) 230.

[43] M. Hernandez, Database Design for Mere Mortals: A Hands-On Guide to Relational Database Design, 3rd edition, Addison-Wesley Professional, Upper Saddle River, NJ, 2013.

[44] B. Gunjal, Database System: Concepts and Design, 2003.

[45] Y. Zhang, Study on Uniaxial compressive constitutive Relationship and Uniaxial Tensile Behavior of Steel-Polypropylene Hybrid Fiber Reinforced Concrete, Ph.D, Wuhan University, 2010.

[46] G. Mei, Study on Uniaxial Tensile Properties and Constitutive Relation of Steel-polypropylene Hybrid Fiber Reinforced Concrete, Ph.D, Wuhan University, 2014.

[47] D.N. Reshef, Y.A. Reshef, H.K. Finucane, S.R. Grossman, G. McVean, P.J. Turnbaugh, E.S. Lander, M. Mitzenmacher, P.C. Sabeti, Detecting Novel Associations in Large Data Sets, Science. 334 (2011) 1518–1524. https://doi.org/10.1126/science.1205438.

[48] X. Shi, P. Park, Y. Rew, K. Huang, C. Sim, Constitutive behaviors of steel fiber reinforced concrete under uniaxial compression and tension, Construction and Building Materials. 233 (2020) 117316. https://doi.org/10.1016/j.conbuildmat.2019.117316.

[49] Y. Shao, Z. Zhu, A. Mirmiran, Cyclic modeling of FRP-confined concrete with improved ductility, Cement and Concrete Composites. 28 (2006) 959–968. https://doi.org/10.1016/j.cemconcomp.2006.07.009.

[50] L. Lam, J.G. Teng, C.H. Cheung, Y. Xiao, FRP-confined concrete under axial cyclic compression, Cement and Concrete Composites. 28 (2006) 949–958. https://doi.org/10.1016/j.cemconcomp.2006.07.007.

[51] P. Li, Y.-F. Wu, Stress–strain model of FRP confined concrete under cyclic loading, Composite Structures. 134 (2015) 60–71. https://doi.org/10.1016/j.compstruct.2015.08.056.

[52] P. Li, Y.-F. Wu, Y. Zhou, F. Xing, Stress-strain model for FRP-confined concrete subject to arbitrary load path, Compos. Pt. B-Eng. 163 (2019) 9–25. https://doi.org/10.1016/j.compositesb.2018.11.002.

[53] R. Park, M. Priestley, W.D. Gill, Ductility of Square-Confined Concrete Columns, Journal of the Structural Division. 108 (1982) 929–950. https://doi.org/10.1016/0022-1694(82)90165-2.

[54] B.D. Scott, R. Park, M. Priestley, Stress-Strain Behavior of Concrete Confined by Overlapping Hoops at Low and High Strain Rates, Aci Journal. 79 (1982) 13–27. https://doi.org/10.14359/10875.

[55] C.M. Sangha, R.K. Dhir, Strength and complete stress-strain relationships for concrete tested in uniaxial compression under different test conditions, 5 (1972) 361–370. https://doi.org/10.1007/bf02476284.

[56] S. Popovics, A numerical approach to the complete stress-strain curve of concrete, Cement & Concrete Research. 3 (1973) 583–599. https://doi.org/10.1016/0008-8846(73)90096-3.

[57] I.P. Saenz, Discussion of "Equation of the Stress-Strain Curve of Concrete," Aci Journal. 61 (1964).

[58] W. Tsai, Uniaxial Compressional Stress-Strain Relation of Concrete, J. Struct. Eng.-ASCE. 114 (1988) 2133–2136. https://doi.org/10.1061/(ASCE)0733-9445(1988)114:9(2133).

[59] B. Li, L. Xu, Y. Chi, B. Huang, C. Li, Experimental investigation on the stress-strain behavior of steel fiber reinforced concrete subjected to uniaxial cyclic compression, Constr. Build. Mater. 140 (2017) 109–118. https://doi.org/10.1016/j.conbuildmat.2017.02.094.

[60] B. Li, Y. Chi, L. Xu, C. Li, Y. Shi, Cyclic tensile behavior of SFRC: Experimental research and analytical model, Constr. Build. Mater. 190 (2018) 1236–1250. https://doi.org/10.1016/j.conbuildmat.2018.09.140.

[61] M.M. Yassin, Nonlinear analysis of prestressed concrete structures under monotonic and cyclic loads., University of California, Berkeley., 1994. https://www.zhangqiaokeyan.com/academic-degree-foreign_mphd_thesis/02061482717.html (accessed October 7, 2022).

[62] I. Goodfellow, Y. Bengio, A. Courville, Deep Learning, Illustrated edition, The MIT Press, Cambridge, Massachusetts, 2016.

[63] Y. LeCun, Y. Bengio, G. Hinton, Deep learning, Nature. 521 (2015) 436–444. https://doi.org/10.1038/nature14539.

[64] S. Bos, E.S. Chng, Using weight decay to optimize the generalization ability of a perceptron, in: Icnn - 1996 Ieee International Conference on Neural Networks, Vols. 1-4, I E E E, New York, 1996: pp. 241–246.

[65] T. Fushiki, Estimation of prediction error by using K-fold cross-validation, Stat. Comput. 21 (2011) 137–146. https://doi.org/10.1007/s11222-009-9153-8.

[66] A. Cernezel, I. Rozman, B. Brumen, Comparisons between Three Cross-Validation Methods for Measuring Learners' Performances, in: B. Thalheim, H. Jaakkola, Y. Kiyoki, N. Yoshida (Eds.), Information Modelling and Knowledge Bases Xxvi, Ios Press, Amsterdam, 2014: pp. 77–87. https://doi.org/10.3233/978-1-61499-472-5-77.

[67] T.-T. Wong, P.-Y. Yeh, Reliable Accuracy Estimates from k-Fold Cross Validation, IEEE Trans. Knowl. Data Eng. 32 (2020) 1586–1594. https://doi.org/10.1109/TKDE.2019.2912815.

[68] Kurniabudi, D. Stiawan, Darmawijoyo, M.Y. Bin Idris, S. Defit, Y.S. Triana, R. Budiarto, Improvement of attack detection performance on the internet of things with PSO-search and random forest, Journal of Computational Science. 64 (2022) 101833. https://doi.org/10.1016/j.jocs.2022.101833.

[69] A.K. Adepu, S. Sahayam, U. Jayaraman, R. Arramraju, Melanoma classification from dermatoscopy images using knowledge distillation for highly imbalanced data, Computers in Biology and Medicine. 154 (2023) 106571. https://doi.org/10.1016/j.compbiomed.2023.106571.

[70] R. Priyadarshini, H. Joardar, S.K. Bisoy, T. Badapanda, Crystal structural prediction of perovskite materials using machine learning: A comparative study, Solid State Communications. 361 (2023) 115062.

https://doi.org/10.1016/j.ssc.2022.115062.

[71] F. Pedregosa, G. Varoquaux, A. Gramfort, V. Michel, B. Thirion, O. Grisel, M. Blondel, P. Prettenhofer, R. Weiss, V. Dubourg, J. Vanderplas, A. Passos, D. Cournapeau, M. Brucher, M. Perrot, É. Duchesnay, Scikit-learn: Machine Learning in Python, Journal of Machine Learning Research. 12 (2011) 2825–2830.

[72] Melo, G.L. De, Fernandes, André L. T., Evaluation of empirical methods to estimate reference evapotranspiration in Uberaba, State of Minas Gerais, Brazil, Engenharia Agrícola. (2012). https://doi.org/10.1590/S0100-69162012000500007.

[73] A.P. Camargo, P. Sentelhas, Avaliação do desempenho de diferentes métodos de estimativa da evapotranspiração potencial no Estado de São Paulo, Brasil, Revista Brasileira de Agrometeorologia. 5 (1997) 89–97.